



This is the accepted manuscript made available via CHORUS. The article has been published as:

Particle-tracking simulation of fractional diffusion-reaction processes

Yong Zhang and Charalambos Papelis

Phys. Rev. E **84**, 066704 — Published 20 December 2011

DOI: [10.1103/PhysRevE.84.066704](https://doi.org/10.1103/PhysRevE.84.066704)

PARTICLE-TRACKING SIMULATION OF FRACTIONAL DIFFUSION-REACTION PROCESSES

YONG ZHANG AND CHARALAMBOS PAPELIS

ABSTRACT. Computer simulation of reactive transport in heterogeneous systems remains a challenge, due to the multi-scale nature of reactive dynamics and the non-Fickian behavior of transport. This study develops a fully Lagrangian approach via particle tracking to describe the reactive transport controlled by the tempered super- or sub-diffusion. In the particle-tracking algorithm, the local-scale reaction is affected by the interaction radius between adjacent reactants, whose motion can be simulated by the Langevin equations corresponding to the tempered stable models. Lagrangian simulation results show that the transient super-diffusion enhances reaction by enhancing the degree of mixing of reactants. The proposed particle-tracking scheme can also be extended conveniently to multi-scaling super-diffusion. For the case of transient sub-diffusion, the trapping of solutes in the immobile phase can either decrease or accelerate the reaction rate, depending on the initial condition of reactant particles. Further practical applications show that the new solver efficiently captures bimolecular reactions observed in laboratories.

1. INTRODUCTION

Efficient simulation of diffusion-controlled chemical reactions in natural systems (such as heterogeneous geological media) remains a challenge, as reviewed recently by Dentz *et al.* [1]. Firstly, reactive transport is a multi-scale process, including the pore-scale process of reactions and the concurrent transport process that evolves with the scale of media [2]. The multi-scale process of reactive transport challenges

Key words and phrases. Anomalous diffusion, Lagrangian approach, Bimolecular reaction, Interaction radius, Fractional diffusion equation.

This work was supported by the National Science Foundation (NSF) under grant DMS-1025417. This paper does not necessarily reflect the views of NSF. Y.Z. thanks the helpful discussion with Dr. Mark M. Meerschaert. We also thank five anonymous reviewers for their insightful suggestions which improved this work.

the application of standard Eulerian solvers that are typically valid at the macroscopic or Darcy scale, since they cannot capture the incomplete mixing of reactants at the microscopic scale [3, 4, 5], unless the reaction rate can be upscaled appropriately [6].

The second difficulty in modeling reactive transport is due to the non-Fickian behavior of transport in real systems. Transport processes in heterogeneous or even some “homogeneous” media are usually anomalous, whose behavior cannot be simulated efficiently by classical transport models assuming Fickian diffusion [7, 8]. Indeed, dispersion of aqueous tracers in natural systems including heterogeneous soils, aquifers, and rivers, is typically found to be non-Fickian [9, 10, 11]. Non-Fickian transport may be characterized by non-Gaussian leading or trailing edges of a plume emanating from a point source, or nonlinear growth of the centered second moment. If the growth rate is faster than linear, the transport is anomalous super-diffusion; slower than linear growth rate is sub-diffusion. Super-diffusion is well-known to be described efficiently by the space fractional-order partial differential equation (PDE) [7], and sub-diffusion can be captured by the time fractional PDE [12].

This study develops numerical algorithms to simulate reactive transport through heterogeneous systems, where the anomalous transport is described by the generalized, space or time fractional PDE. Lagrangian numerical solvers are selected because they show promising advantages in simulating the interaction between reaction and transport [13, 14], due to the discrete nature of particles in the typical Lagrangian solver [15, 16]. The Lagrangian approach is a downscaling technique that can characterize both reactions and transport at the same scale, and it is expected to overcome the above two computational difficulties. For description simplicity, we focus only on reactive transport in porous media. The resultant numerical method can be extended to similar physical processes in other media (such as reactions in the gas phase).

The rest of the paper covers methodology development, numerical result analysis and validation, and real-world applications. In Sec. 2, the irreversible and reversible bimolecular chemical reaction combined

with the transient super-diffusion is modeled by a Lagrangian framework. Numerical results are compared to and validated by known kinetics of reactions. The numerical method can be extended conveniently to multi-dimensional transport processes. In Sec. 3, additional steps of particle-tracking algorithms are added to capture chemical reactions combined with the transient sub-diffusion, where particles experience multiple status (i.e., mobile versus immobile status). In Sec. 4, the applicability of the resultant particle-tracking schemes is checked systematically against laboratory measurements of bimolecular reactions. Future extension of the Lagrangian solver is then discussed briefly in Sec. 5. Conclusions are drawn in Sec. 6. The computer generation of tempered stable random variables, which is critical to the Lagrangian solver developed in this study, is discussed in Appendix A. In addition, to cross-verify the Lagrangian simulation of conservative tracer transport (representing the difference between the two reactants), the implicit Eulerian finite difference approximation for the space and time tempered fractional PDE is developed in Appendix B. Two important extensions of the computational approach are also discussed, including the Lagrangian scheme with a nonlinear forward reaction probability in Appendix C and the particle-tracking simulation of the coupled reaction and subdiffusion in Appendix D.

It is also noteworthy that our investigation of reactive transport may be of interest in chemistry, since reaction is one of the fundamental concepts in chemistry. The major focus of this work, however, is the development of Lagrangian description of the dynamic process built upon the Langevin equation and the time-subordination analysis, which belong to the areas of computational and statistical physics. The result of this work may be used not only by chemists, but also by other communities such as hydrologists and engineers. For the convenience of readers without chemical background, in the following we explain the basic chemical terms used in the analysis.

2. LAGRANGIAN SIMULATION OF BIMOLECULAR REACTION CONTROLLED BY THE TEMPERED SUPER-DIFFUSION

Chemical reactions combined with super-diffusive transport are considered first. To illustrate the physical process, we build the continuum

model. The space fractional-order PDE [7, 17, 18] can efficiently capture super-diffusive transport of nonreactive tracers observed in complex, natural geological formations, as reviewed and demonstrated further by Zhang *et al.* [12]. The space tempered stable model [19, 20, 21] is the logic extension of the standard fractional-order PDE to capture the convergent spatial moments and the natural cutoff of power-law distributions present in real physical systems. The model describes the transition from super-diffusion to asymptotic, normal diffusion limits over time. The standard fractional-order PDE and the classical diffusion equation are two end-members of the space tempered stable model. The following fractional-order, advection-dispersion-reaction (ADR) equation may describe the elementary, bimolecular second-order reversible reaction $A + B \rightleftharpoons C$ undergoing tempered super-diffusive transport:

$$(1a) \quad \frac{\partial[A]}{\partial t} = -v_A \frac{\partial[A]}{\partial x} + D_A \frac{\partial^{\alpha, \lambda}[A]}{\partial x^{\alpha, \lambda}} - K_f^*[A][B] + K_r^*[C] ,$$

$$(1b) \quad \frac{\partial[B]}{\partial t} = -v_B \frac{\partial[B]}{\partial x} + D_B \frac{\partial^{\alpha, \lambda}[B]}{\partial x^{\alpha, \lambda}} - K_f^*[A][B] + K_r^*[C] ,$$

$$(1c) \quad \frac{\partial[C]}{\partial t} = -v_C \frac{\partial[C]}{\partial x} + D_C \frac{\partial^{\alpha, \lambda}[C]}{\partial x^{\alpha, \lambda}} + K_f^*[A][B] - K_r^*[C] ,$$

where v_i [LT^{-1}] is the mean flow velocity, D_i [$L^\alpha T^{-1}$] is the macroscopic dispersion coefficient ($i = A, B, C$ denotes reactant A , reactant B , and product C , respectively), K_f^* [$M^{-1}L^3T^{-1}$] and K_r^* [T^{-1}] are the *upscaled*, forward and backward kinetic coefficient of reaction, respectively, and $[A]$, $[B]$ and $[C]$ [ML^{-3}] denote the concentration of A , B , and C , respectively. The operator $\frac{\partial^{\alpha, \lambda}}{\partial x^{\alpha, \lambda}}$ denotes the tempered fractional derivative [19, 20]. For example:

$$(2) \quad \frac{\partial^{\alpha, \lambda}[A]}{\partial x^{\alpha, \lambda}} = e^{-\lambda x} \frac{\partial^\alpha (e^{\lambda x}[A])}{\partial x^\alpha} - \alpha \lambda^{\alpha-1} \frac{\partial[A]}{\partial x} - \lambda^\alpha [A] ,$$

where α [dimensionless] is the order of the space fractional derivative, and λ [L^{-1}] is the truncation parameter in space. The parameters α and λ can be species dependent. When $\lambda \rightarrow 0$ (i.e., no tempering), the ADR model (1) reduces to the one considered by Bolster *et al.* [22]. Here the bimolecular reaction means the elementary reaction where two

molecules (A and B) collide and react with each other. The second-order reaction means that the sum of the power in the concentration term in the rate equation is equal to 2.

Note that the continuum, averaged concentration model (1) merges the mixing at local scale (where reactions occur) and the spreading at the Darcy scale [2]. In other words, the macroscopic chemical behavior is described by means of a kinetic reaction rate [6]. Therefore, the rate coefficients K_f^* and K_r^* must be obtained by upscaling K_f (the microscopic forward rate coefficient) and K_r (the microscopic backward rate coefficient), respectively. How to efficiently upscale the rate coefficients remains a challenge, if not impossible. The fact, however, is that K_f (or K_r) can be measured conveniently in the laboratory. This discrepancy motivated us to develop alternative, efficient Lagrangian solvers by *downscaling* the transport, so that there is no need to up-scale chemical reactions and the laboratory measurement of K_f can be used directly. Similar *downscaling* approaches have been proposed recently, by focusing on the Fickian diffusion [3, 23, 24] or the time nonlocal transport process [13, 14]. The Lagrangian simulation of reactive transport with the tempered super-diffusion or the sub-diffusion with mobile/immobile phases discussed below remains unknown.

In the following we consider two common systems - the closed system and the open system, where the Lagrangian simulation of chemical reactions can differ slightly. The closed system represents a bounded domain with a constant volume. It is filled with reactants. Analytical solutions for reactive dynamics had been derived for the assumption of perfect mixing of reactants (or instantaneous equilibrium where the reaction reaches a state of balance instantaneously when one reactant particle A meets any reactant particle B), providing background to compare with the Lagrangian solutions of reaction rate.

In the open system considered in this study, there is no overlap between different reactants at the beginning and the volume of mixed reactants can increase with time. In laboratory experiments of bimolecular reactions [4, 5, 25], the two reactants A and B typically have a sharp contact initially. One reactant was usually introduced separately into the saturated porous medium (i.e., sand column) filled with another reactant. This common case is an open system filled with initially

non-overlapping reactants. The open system is practically important since it provides the experimental data to check the applicability of the Lagrangian simulator.

2.1. Particle tracking algorithm development. To efficiently characterize the dynamics of chemicals undergoing super-diffusive, reactive transport, there are four main steps of the Lagrangian solver discussed in the following four subsections. The backward reaction, the displacement of each species, and the forward reaction, are simulated separately. The similar separation was also proposed by Zhang [24] for reactive transport with Fickian diffusion.

2.1.1. Step 1: Probability-based approximation of the backward reaction $C \rightarrow A + B$. The backward reaction probability P_b is [24]

$$(3) \quad P_b = \frac{|\Delta[C(t)]|}{[C(t)]} = K_r \Delta t ,$$

where Δt ($0 < \Delta t < 1/K_r$) is the time step, and $\Delta[C(t)]$ denotes the change in concentration of product C during the small time step Δt . If Δt is small enough, the backward probability (3) results in the rate equation for backward reaction:

$$(4) \quad \left| \frac{\partial[C(t)]}{\partial t} \right| \approx K_r [C(t)] .$$

In the particle tracking scheme, a uniform $[0 \ 1]$ random number W [dimensionless] is generated and compared with P_b . If $W > P_b$, then no backward reaction can occur; if $W \leq P_b$, the product particle transforms to reactants.

2.1.2. Step 2: The Langevin equation based simulation of the tempered super-diffusive transport for each species. We then apply the following Langevin equation to describe the random, tempered super-diffusive movement of reactants (and the mobile product) during the i -th time step [26]:

$$(5) \quad dX_i = v \Delta t_i + D \alpha \lambda^{\alpha-1} \Delta t_i + d\xi_i ,$$

where $d\xi_i$ [L] is a tempered α -order stable random variable representing the random dispersion noise. $d\xi_i$ can be generated using the method discussed in Appendix A. The corresponding governing

equation for solute displacement is a spatially tempered, fractional advection-dispersion equation (FADE) [26]:

$$(6) \quad \frac{\partial P(x, t)}{\partial t} = -v \frac{\partial P(x, t)}{\partial x} + D \left\{ e^{-\lambda x} \frac{\partial^\alpha [e^{\lambda x} P(x, t)]}{\partial x^\alpha} - \alpha \lambda^{\alpha-1} \frac{\partial P(x, t)}{\partial x} - \lambda^\alpha P(x, t) \right\}.$$

It is noteworthy that the Langevin equation (5) describes a microscopic, random-walk process [7], while the continuum model (6) is the scaling limit of the random walks [26, 27].

2.1.3. *Step 3: Simulation of the forward reaction $A + B \rightarrow C$ controlled by interaction radius R .* There are different ways to simulate the forward reaction, where the most efficient one is to use the following probability P_f^* for each pair of reactants [24]:

$$(7) \quad P_f^*(t) = 1 - \frac{|y_{A,i}(t) - y_{B,j}(t)|}{R},$$

where $y_{A,i}(t)$ and $y_{B,j}(t)$ [L] denote the position of the i -th A particle ($1 \leq i \leq N_A(t)$) and the j -th B particle ($1 \leq j \leq N_B(t)$), respectively; $N_A(t)$ and $N_B(t)$ [dimensionless] are the remaining number of A and B particles at time t , respectively; and R [L] denotes the interaction radius which defines the maximum distance where two reactants may collide and then react. In this manuscript we will check whether the simple linear form (7) can generate the correct reaction rate, and whether it is applicable in real-world applications. Other forms of $P_f^*(t)$ are certainly possible and will be discussed in Appendix C. Interested readers may select the form they prefer.

Similar to Step 1, here another uniform [0 1] random number W^* is generated. If $W^* > P_f^*$, then no forward reaction can occur; otherwise A and B particles combine to produce a C particle. Therefore, if the distance between A and B particles is larger than the interaction radius R , $P_f^* < 0$ and hence no forward reaction can occur. When the two different species are closer than R , the forward reaction will occur if $W^* \leq P_f^*$. The resultant average forward probability $\bar{P}_f(t)$ for all reactants, as derived by Zhang [24], is

$$(8) \quad \bar{P}_f(t) \approx \frac{R}{L/N_A(t)},$$

where L is the length of the system (for the one-dimensional or 1- d medium).

For the case of the closed system with well-mixed reactants, the interaction radius should be the same as the one for Fickian transport [24], since the rate equation for bimolecular reactions in a closed system is not altered by the super-diffusive displacement of particles. Zhang [24] found that the interaction radius (denoted as R_C , where the suffix “C” represents the closed system) can be predicted by

$$(9) \quad R_C = \frac{K_f [A_0] L \Delta t}{N_A^0},$$

where $[A_0]$ is the initial concentration of A , and N_A^0 is the initial number of A particles at time $t = 0$.

To see how the forward reaction probability $\bar{P}_f(t)$ (8) relates to the interaction radius R_C , we can define this probability as the relative variation of particle numbers or concentration for reactant A :

$$(10) \quad \bar{P}_f(t) = \frac{\Delta N_A}{N_A(t)} = \frac{\Delta[A(t)]}{[A(t)]},$$

where $\Delta[A(t)]$ is the change in concentration of A . The relative change of concentration, as expressed by $\Delta[A(t)]/[A(t)]$ in (10), can also be related to the volume occupied by reactant particles [28, 29]

$$(11) \quad \frac{\Delta[A(t)]}{[A(t)]} = \frac{V_i}{V} = \frac{R_C N_A(t)}{L},$$

where V is the total spatial volume (which equals to the closed domain size L in the 1- d case), V_i is the proportion of volume in V where A interacts with B , and the interaction radius R accounts for the reaction volume assigned to each reactant particle. Leading (11) into (10), we obtain the forward reaction probability (8).

To see how the interaction radius R_C takes the form of (9), we illustrates the forward reaction with equivalent initial concentrations between A and B (i.e., $[A_0] = [B_0]$). The well-known rate equation for this case is

$$(12) \quad \frac{\partial[A(t)]}{\partial t} = -K_f [A(t)]^2.$$

Substituting (12) into (11) results in

$$(13) \quad R_C = \frac{\Delta[A(t)]}{[A(t)]} \frac{L}{N_A(t)} \approx \frac{K_f [A(t)] L \Delta t}{N_A(t)}.$$

Because $[A(t)]/N_A(t) = [A_0]/N_A^0$ (since each particle contains the same amount of mass), the interaction radius defined by (13) is the same as (9).

2.1.4. Step 4: Iteration. There are two loops in the above Lagrangian scheme. The outer loop iterates time, and the inner loop calculates the reactive transport for each particle by iterating on the above three steps. In the following we test and apply the 4-step Lagrangian scheme.

2.2. Validation and numerical examples. We first check extensively the above Lagrangian solver by evaluating the concentration difference between A and B , denoted as $[u(x, t)] = [A(x, t)] - [B(x, t)]$. The governing equation for $[u(x, t)]$ is the difference between Eq. (1a) and (1b). Therefore, $[u(x, t)]$ can be regarded as the concentration of a conservative tracer (if $v_A = v_B$ and $D_A = D_B$), where the transport is governed by the tempered stable model (6). For cross-verification, we also develop the Eulerian solver (Appendix B) to approximate the model (6) and its extension. This provides an indirect way to check the Lagrangian solver proposed above. Numerical examples shown in Fig. 1 reveal that the Lagrangian solution generally matches the Eulerian solution, although the former contains more noise due to the discrete nature of particle-based approaches.

We then apply the above Lagrangian framework to evaluate the chemical kinetics. One example is shown in Fig. 2. The decline of mass for reactant A is affected by the scale index α (Fig. 2a) and the truncation parameter λ (Fig. 2b). For the case of Fickian diffusion (corresponding to $\alpha \rightarrow 2$ or $\alpha = 1.99$ in Fig. 2), the normalized concentration $[A(t)]/[A_0]$ grows as $t^{-1/4}$ at later time. With the decrease of α , reactant particles have a higher probability to experience large jumps, resulting in an enhanced mixing between reactants. Or in other words, particles of different species have a higher chance to collide (or “meet”) and then react. The decline of $[A(t)]/[A_0]$ therefore accelerates at later time, as shown by Fig. 2a. Similar behavior is observed

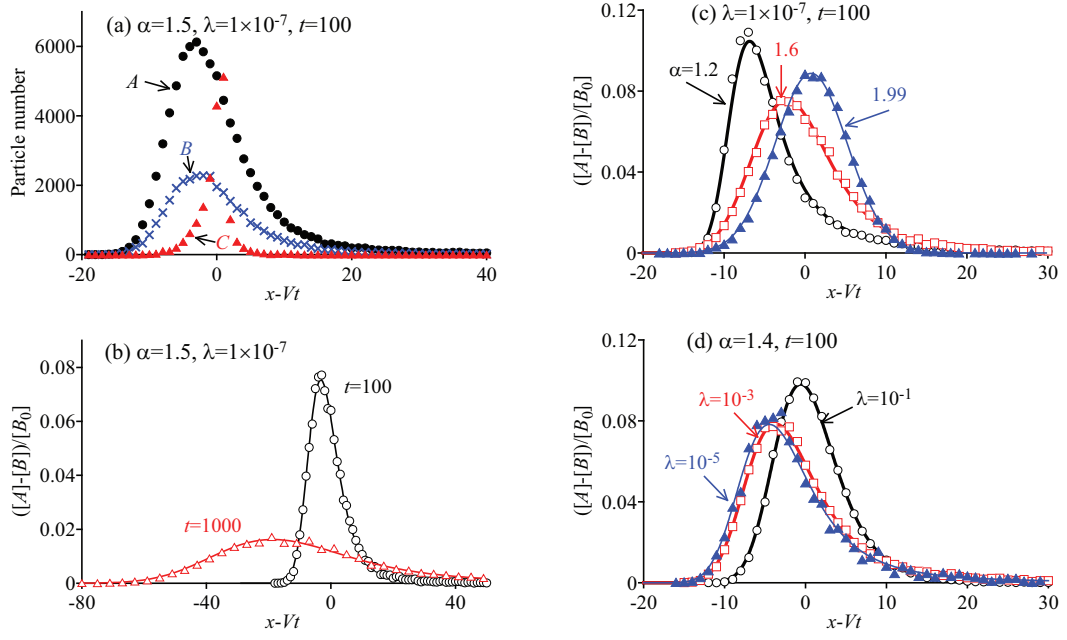


FIGURE 1. (Color online) Snapshots for *irreversible* reaction $A + B \rightarrow C$. The displacement of particles follows the space FADE (6). (a) Lagrangian solution of the snapshot for reactants $[A]$ and $[B]$, and product $[C]$. Model parameters are: $\alpha = 1.5$, $\lambda = 1 \times 10^{-7}$, and $t = 100$. (b) Snapshots of $[A] - [B]$ at time $t = 100$ and $t = 1000$, respectively. (c) The influence of scale index α on the snapshot of $[A] - [B]$. (d) Influence of the truncation parameter λ on the snapshot of $[A] - [B]$. In (b)~(d), symbols are the Lagrangian solutions, and lines are the implicit Eulerian finite difference solutions.

when the truncation parameter λ decreases (Fig. 2b), since a small λ represents relatively larger displacements for particles.

Numerical examples also show that the simulated reaction rate increases with the increase of particle numbers (denoted as np) and/or the dispersion coefficient (D). This behavior is consistent with the conclusion drawn by Benson and Meerschaert [3]. As shown in Fig. 2, the Lagrangian solution of $[A(t)]$ with a large np and/or D can be close to the analytical solution for perfect mixing. Therefore, the chemical reaction with Fickian diffusion and the chemical reaction with perfect

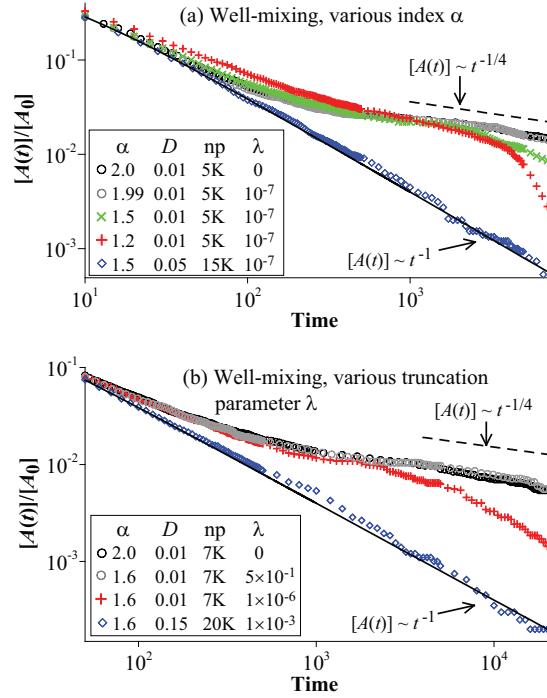


FIGURE 2. (Color online) Mass evolution for the bimolecular *irreversible* reaction $A + B \rightarrow C$ in a closed system, where the transport of chemicals is described by the spatially tempered, fractional advection-dispersion equation (6). Symbols are the Lagrangian solutions, and the solid line is the analytical solution assuming perfect mixing. (a) shows the influence of scale index α on the mass decline of reactant A . Other model parameters are: $K_f = 50$, and $[A_0] = 0.005$. Note that the solution of $\alpha = 1.99$ is almost identical to the case of the standard 2nd-order advection-dispersion equation (ADE) (i.e., $\alpha = 2$ and $\lambda = 0$ in (6)). (b) shows the influence of truncation parameter λ on the mass decline of reactant A . Other model parameters are: $K_f = 50$ and $[A_0] = 0.005$. Note that the solution of $\lambda = 0.5$ is almost identical to the case of ADE.

mixing are the two bounds of chemical reactions with the tempered super-diffusion.

Fig. 3 shows the case of a *reversible* reaction. The Lagrangian solution tends to converge to the analytical solution assuming perfect mixing. The concentration of reactant A becomes constant at later

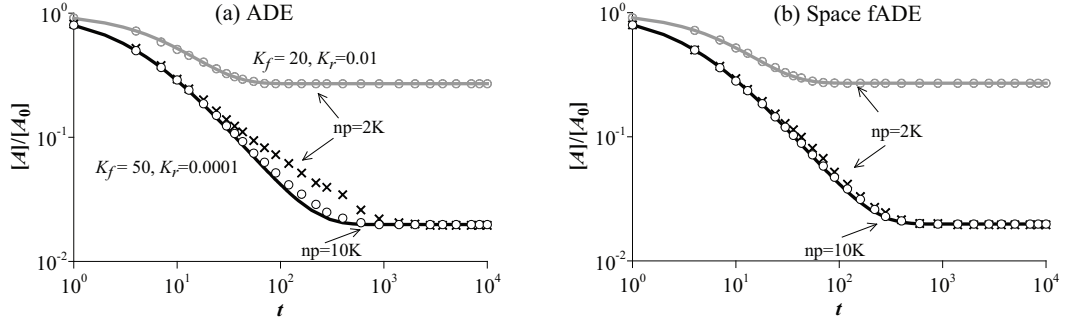


FIGURE 3. Mass evolution of reactant A for the *reversible* reaction $A + B \rightleftharpoons C$ in a closed system, where the transport model is ADE (a) or the space tempered FADE (6) (b). The two lines are the analytical solutions by assuming perfect mixing, where the grey line denotes the reaction with the forward rate $K_f = 20$ and the backward rate $K_r = 0.01$, and the black line with $K_f = 50$ and $K_r = 0.0001$. The symbols are the Lagrangian solutions, where “np” denotes the number of particles. The other model parameters are: $D = 0.1$ and $[A_0] = 0.005$. In the space tempered FADE model (b), $\alpha = 1.8$ and $\lambda = 1 \times 10^{-7}$.

time when the *reversible* reaction reaches dynamic equilibrium. In the Lagrangian simulation developed above, the state of equilibrium is characterized by similar number of particles undergoing backward reaction (Step 1 in Subsec. 2.1.1) and forward reaction (Step 3 in Subsec. 2.1.3) in the same time step, where the net reaction rate is close to zero. Fig. 3 also shows that the tempered super-diffusion enhances the reaction.

2.3. Extension to the open system. For the open system with sharp-interface between reactants, the interaction radius (denoted as R_O , where the suffix “O” represents the open system) differs from (9) or (13). It is because only the reactants around the sharp interface can react, while the definition (9) or (13) assumes that all reactants in the system can react (and hence every reactant particle can be assigned an interaction radius).

Edery *et al.* [13, 14] treated the interaction radius as a constant that can be fitted by measurements. This method can be adopted easily

in the above Lagrangian scheme. One numerical example is shown in Fig. 4b. Compared to Fickian diffusion (Fig. 4a), the leading edge of the product C due to super-diffusion is apparent. The heavy leading edge of the invading reactant A increases the reaction between A and the displaced (background) reactant B . Hence, for the open system, the tempered super-diffusive transport enhances reaction rate, similar to that observed in the closed system.

The second method is to extend the following empirical formula for interaction radius proposed by Zhang [24] for normal diffusion:

$$(14) \quad R_O(t) \approx \frac{K_f [A_0] L \Delta t}{N_A^0} \frac{L}{\sqrt{2Dt}} \text{Re},$$

where $R_O(t)$ changes with time, and Re denotes the Reynolds number. The term $L/\sqrt{2Dt}$ accounts for the variation of the mixing volume of reactants, and the Reynolds number captures the influence of flow velocity on the interaction radius. For simplicity, we consider here only the *irreversible* reaction. The spreading rate of plume for super-diffusion differs significantly from normal diffusion. This motivates us to update (14) to:

$$(15) \quad R_O(t) \approx \frac{K_f [A_0] L \Delta t}{N_A^0} \frac{L}{\sqrt{D\alpha(\alpha-1)\lambda^{\alpha-2}t}} \text{Re},$$

where $\sqrt{D\alpha(\alpha-1)\lambda^{\alpha-2}t}$ is the variance of displacement for particles governed by the space tempered PDE (6). When $\alpha = 2$, (15) reduces to (14).

The empirical formula (15) is used in the numerical example shown in Fig. 4c. The solid line in Fig. 4c is the mixing zone between reactants A and B , when there is no reaction. Fig. 4d shows that the peak concentration of the mixing zone is half of the initial concentration for reactants, similar to the case of Fickian diffusion (see [4]). The product concentration is below this mixing zone, just as expected (because not all reactants in this zone can react).

In real applications, R_O can be used as either a constant or a time-dependent variable (15). The former is more convenient, while the latter contains variables with solid physical meanings. In the following real applications (Sec. 4), we will test first the applicability of (15), followed by a fitting parameter for R_O if (15) fails.

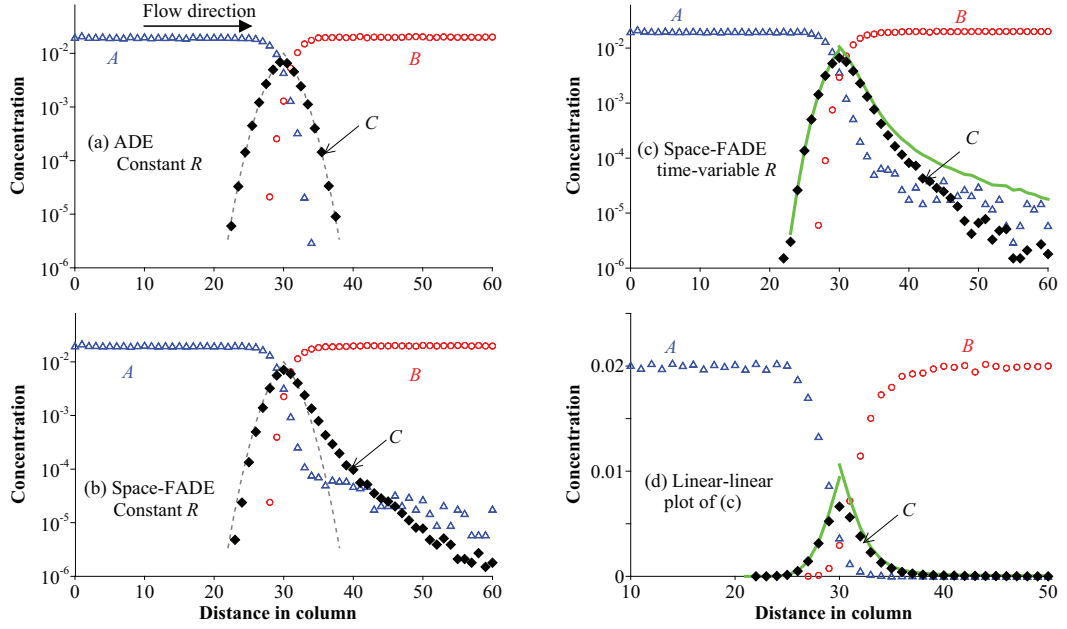


FIGURE 4. (Color online) Open system: the simulated snapshot (symbols) for A , B and C , where the diffusion is governed by the ADE (a) or the tempered space FADE (6) ((b)~(d)). In all cases, the common parameters are: $L = 60$, $K_f = 1$, $v = 0.6$, $D = 0.05$, $[A_0] = [B_0] = 0.02$, $[C_0] = 0$, $T = 50$, time step $dt = 1$, and the particle number is $np = 400,000$. The dashed line in (a) and (b) denotes the analytical solution by assuming perfect mixing for the ADE model. In (c), the solid line denotes the concentration of A and B in the mixing zone (without reaction). In the tempered space FADE ((b)~(d)), additional parameters are: $\alpha = 1.8$ and $\lambda = 0.0001$. (a) and (b) assumes the constant interaction radius $R = 0.00007$, while (c) uses the empirical, time-dependent R_O (15).

2.4. Extension to multi-dimensional super-diffusion. Real-world transport processes can be multi-dimensional. The following model describes the multi-scaling, tempered FADE [30]

$$(16) \quad \frac{\partial}{\partial t} P(\vec{x}, t) = -v \nabla P(\vec{x}, t) + \mathbf{D} \cdot \nabla_M^{\mathbf{H}^{-1}, \vec{\lambda}} [P(\vec{x}, t)] ,$$

where \mathbf{D} is the dispersion tensor, \mathbf{H}^{-1} is the inverse of the scaling matrix defining the order and direction of the space fractional derivatives, $M = M(\theta)$ is the mixing measure specifying the probability of

particle jumps in each direction θ , and $\vec{\lambda}$ defines the truncation parameter along each eigenvector of \mathbf{H} . The operator $\nabla_M^{\mathbf{H}^{-1}, \vec{\lambda}}$ denotes the tempered multiscaling fractional derivative with the Fourier transform

$$F[\nabla_M^{\mathbf{H}^{-1}, \vec{\lambda}}] = \int (e^{-i\vec{k} \cdot \vec{x}} - 1 + i\vec{k} \cdot \vec{x}) e^{-\vec{\lambda} \cdot \overrightarrow{|S^{-1}\vec{x}|}} \phi(d\vec{x}),$$

where $\overrightarrow{|x|} = (|x_1|, |x_2|, \dots, |x_d|)$, $\phi(dy)$ is the Lévy measure with $\phi(d\vec{x}) = r^{-2} dr M(d\theta)$, $\vec{x} = r^{\mathbf{H}} \theta$ and $\mathbf{H} = \mathbf{S} \mathbf{H}_0 \mathbf{S}^{-1}$ (where \mathbf{S} and \mathbf{H}_0 are eigenvector and eigenvalue matrices).

The vector Langevin approach developed by Zhang *et al.* [31] can be used to approximate the vector model (16), where the relationship between the weights of $M(\theta)$ and the eigenvectors of \mathbf{H} describes the dependence structure of the solute plume. This vector Langevin approach replaces Step 2 proposed in Subsec. 2.1.2, while the other steps need not to be changed in the Lagrangian solver.

Fig. 5 shows one example of such extension. No other solution is available for chemical reactions with vector fractional diffusion. Hence the example shown in Fig. 5 can not be cross verified.

3. LAGRANGIAN SIMULATION OF BIMOLECULAR REACTION CONTROLLED BY THE TEMPERED SUB-DIFFUSION

The following time tempered fractional advection-dispersion equation proposed by Meerschaert *et al.* [21] captures the transient anomalous diffusion:

$$(17a) \quad \frac{\partial C_T}{\partial t} + \beta e^{-st} \frac{\partial^\gamma}{\partial t^\gamma} (e^{st} C_T) - \beta s^\gamma C_T = L_x C_T + m_0 \beta g(t) \delta(x),$$

$$(17b) \quad \frac{\partial C_M}{\partial t} + \beta e^{-st} \frac{\partial^\gamma}{\partial t^\gamma} (e^{st} C_M) - \beta s^\gamma C_M = L_x C_M,$$

where C_T and C_M denote tracer concentration in the total (mobile + immobile) and mobile phases, respectively, γ ($0 < \gamma < 1$) [dimensionless] is the scale index, L_x is the advection-dispersion operator, β [$T^{\gamma-1}$] is the capacity coefficient, $\delta(x)$ is the Dirac delta function, m_0 [ML^{-3}] is the initial mass, $g(t)$ [$T^{-\gamma}$] denotes the memory function, and s [T^{-1}] denotes the truncation parameter in time. When $s \rightarrow 0$ (i.e., no tempering), model (17) reduces to the standard, fractal mobile/immobile

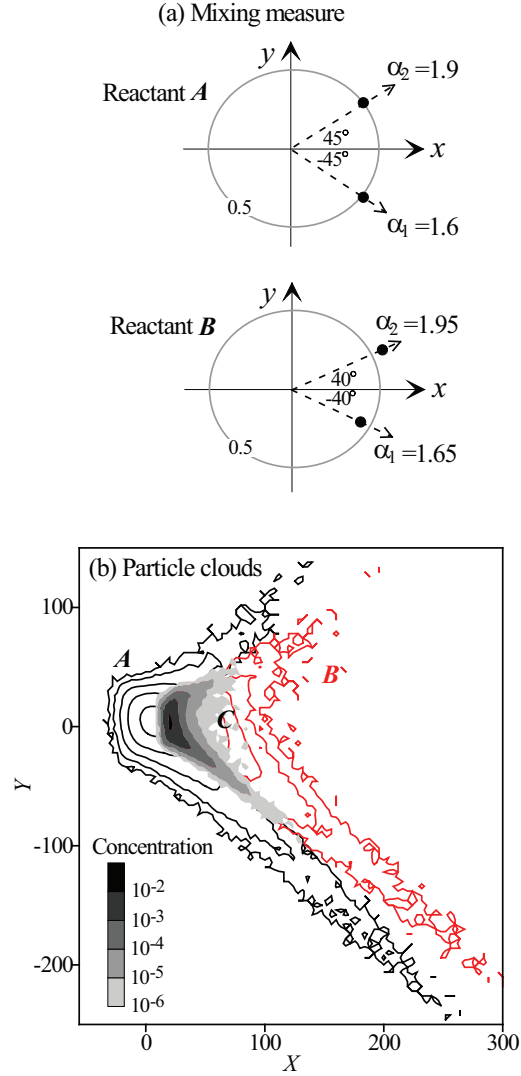


FIGURE 5. (Color online) 2- d tempered super-diffusion with reaction $A + B \rightarrow C$: (a) The mixing measure for reactant A and B , respectively. (b) The simulated particle clouds (i.e., the plume snapshot) at time $t = 10$. The velocity is $v_x = 1$, $v_y = 0$. The dispersion coefficient is $D_1 = D_2 = 7$ (where “1” and “2” denotes the jump direction shown in (a)) for reactant A , and $D_1 = D_2 = 7.5$ for reactant B . The initial point source location for A and B is $(0, 0)$ and $(30, 0)$, respectively. The truncation parameter λ along the two directions (“1” and “2”) is 0.006 and 0.01, respectively. The interaction radius (of a circle) is 2.

model [12]

$$(18a) \quad \frac{\partial C_T}{\partial t} + \beta \frac{\partial^\gamma C_T}{\partial t^\gamma} = L_x C_T + m_0 \beta g(t) \delta(x) ,$$

$$(18b) \quad \frac{\partial C_M}{\partial t} + \beta \frac{\partial^\gamma C_M}{\partial t^\gamma} = L_x C_M ,$$

where the memory function $g(t) = t^{-\gamma}/\Gamma(1-\gamma)$, $\Gamma(\cdot)$ is the Gamma function, and $\partial^\gamma/\partial t^\gamma$ denotes the Riemann-Liouville fractional derivative of order γ . Hence the time tempered FADE model (17) contains the standard model (18) as a special case.

In the following, we develop the Lagrangian solution for reactive transport where the transport component is described by model (17). The resultant Lagrangian solver may also be extended for other types of time-fractional PDE, including model (18) or the classical time-fractional derivative model [7]

$$(19) \quad \frac{\partial^\gamma P(x, t)}{\partial t^\gamma} = -v \frac{\partial P(x, t)}{\partial x} + D \frac{\partial^2 P(x, t)}{\partial x^2} .$$

Also note that, strictly speaking, the time-fractional derivative models do not produce pure sub-diffusion if the advection component dominates [32]. However, model (17) describes the trapping of solute particles in immobile domains, representing a delayed transport. Hence, for description simplicity, we name the resultant transport as a sub-diffusive process, to keep consistent to the terminology used before [12].

3.1. The closed system. For simplicity, this Subsec. considers a pure diffusive process (which is also a sub-diffusive process) in a closed system. Particles representing reactants stay in either mobile or immobile phases, where the total time and the rate equation are the same as those for normal diffusion. Therefore, the interaction radius follows the same analytic solution (9).

A Lagrangian scheme is developed by extending the time-subordination approach proposed by Magdziarz and Weron [33], as shown in Fig. 6. It contains the following six major steps.

Step 1: Convert the operational time spent by each particle during the j -th jump to the clock time via the following Langevin equation

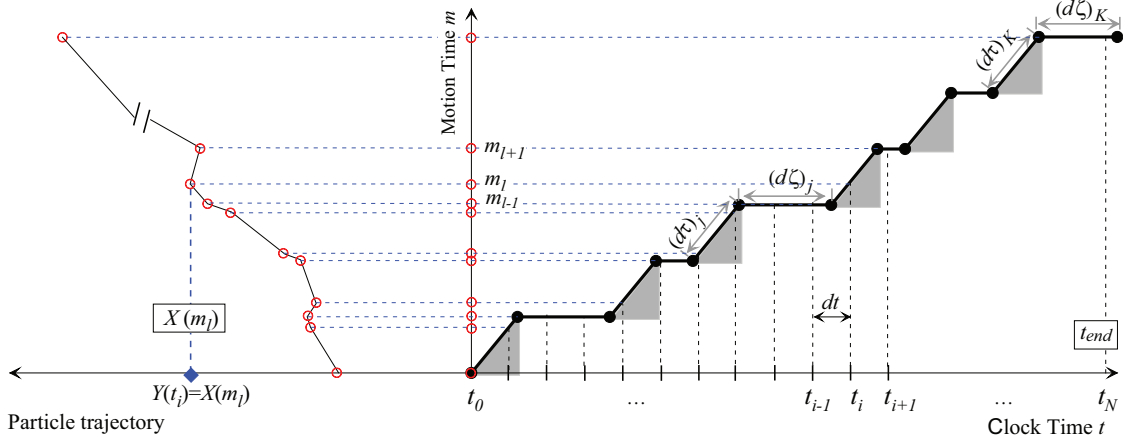


FIGURE 6. (Color online) Schematic process of the time-subordination approach. The right-side of the vertical axis shows the relationship between clock time t and motion time m . The shaded and the blank areas represent mobile and immobile phases, respectively. t_{end} is the whole modeling time. The discretization of the clock time $t(m)$ can have a uniform interval dt (shown by the vertical dotted lines), while the motion time $m(t)$ has a non-uniform interval dm_k (shown by the horizontal dotted lines). The left-side of the vertical axis shows the particle trajectory corresponding to each motion time m_l (where $l = 0, 1, \dots, L$). The time-subordination approach shows that $Y(t_i) = X(m_l)$.

[21]:

$$(20) \quad dT_j = d\tau_j + d\zeta_j,$$

where dT_j denotes the clock (also called the physical or real) time, $d\tau_j$ is the predefined operational time step (which can be a constant), and $d\zeta_j$ is a tempered γ -order stable random variable representing the random amount of time a solute particle is trapped in the immobile phase. The time-domain Langevin approach developed by Zhang *et al.* [32] also leads to (20). The computer generation of $d\zeta_j$ is similar to the random number $d\xi_i$ used in the displacement (5) (see Appendix A for details).

Step 2: Discretize the clock time dT_j into a finer resolution with a smaller real time step dt (see the horizontal axis in Fig. 6). Find

the corresponding motion time m_l for each real time point t_i (see the vertical axis in Fig. 6). The real time t_i can be in a regular or irregular mesh, corresponding to the output time.

Step 3: Simulate the displacement $X(m_l)$ during the operational time m_l for each solute particle A , B and C . Particle tracking schemes have already been developed for Fickian diffusion [15] and super-Fickian diffusion [31].

Step 4: Use the time subordination theory to obtain the particle position at clock time t_i [33, 32]:

$$(21) \quad Y(t_i) = X(m_l) = X(\Sigma_{k=1}^{k=l} dm_k) .$$

Step 5: At this clock time t_i , simulate the reaction $A + B \rightarrow C$, using the same methodology developed for super-diffusive reactions (see Subsec. 2.1.3).

Step 6: Repeat Steps 1 \sim 5 till reaching the end t_{end} .

Note that when $d\tau_j = 0$ in the time-Langevin equation (20), the above Lagrangian method simulates the forward reaction with transport governed by the classical time-fractional model (19). A zero operational time $d\tau_j$ implies instantaneous jumps [10], or mobile status all the time [32]. Also note that the backward reaction can be added before Step 1, to simulate the *reversible* reaction.

Examples of the above Lagrangian scheme are shown in Fig. 7. The difference between concentration of A and B , as expressed by $u(x, t) = [A(x, t)] - [B(x, t)]$, represents a conservative tracer whose dynamics is governed by the model (17). We first apply the Lagrangian scheme to approximate the concentration of two reactants A and B . The resultant solution $[A(x, t)] - [B(x, t)]$ is then compared to the implicit Eulerian solution for model (17) (see Appendix B). The two quite different methods generate similar results, for various capacity coefficients β (Fig. 7a,b), indices γ , and truncation parameters s (Fig. 7c,d).

We then evaluate the simulated reaction rate using the Lagrangian solver. Fig. 8a shows the influence of γ on the decline of mass for reactant A . For a smaller γ , there is a higher probability for long-waiting times, decreasing the mobility of reactant particles. The mixing (or collision) of reactants decreases accordingly, resulting in a smaller overall reaction rate. When $\gamma \rightarrow 1$ (i.e., $\gamma = 0.99$), the simulated reactive

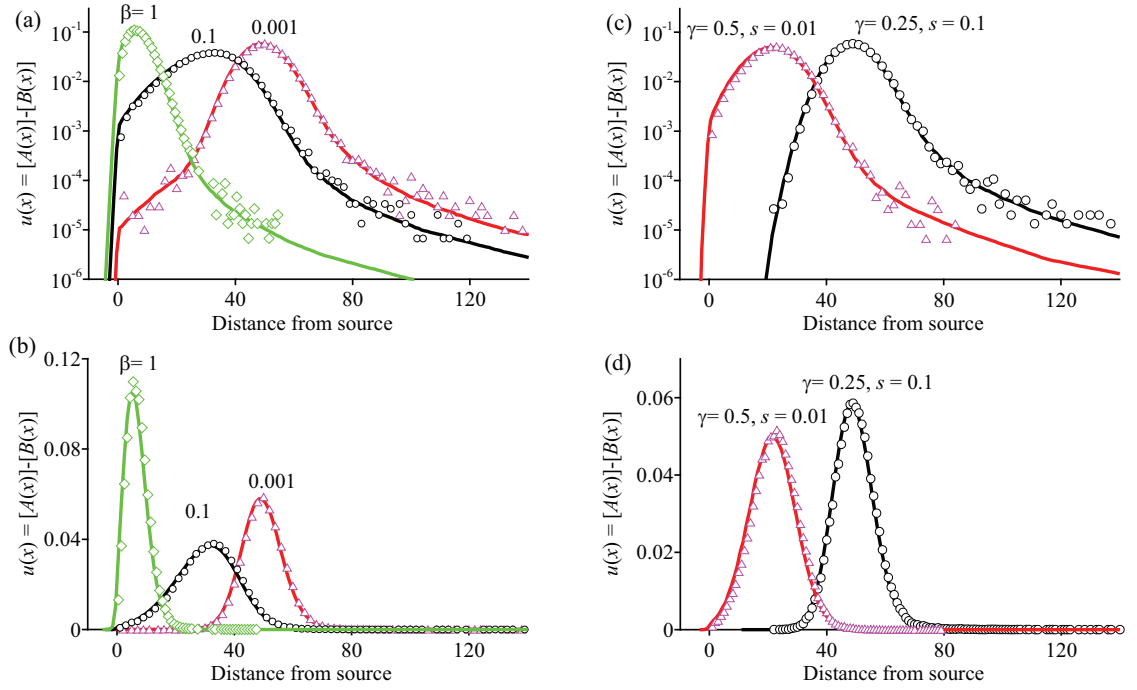


FIGURE 7. (Color online) Lagrangian solutions (symbols) versus Eulerian finite difference solutions (lines) for $u(x, t) = [A(x, t)] - [B(x, t)]$, where the transport of chemicals is described by the time tempered FADE (17) with well-mixed reactants. Model parameters (that are the same for all cases) are: space index $\alpha = 1.9$, $v = 0.25$, $D = 0.1$, $[A_0] = 0.00005$, $[B_0] = 0.000025$, at time $t = 200$. (a) shows various capacity coefficients β . Other model parameters are: time index $\gamma = 0.25$, and time truncation parameter $s = 0.01$. (b) is the linear-linear plot of (a). (c) shows two cases with different time indices γ and time truncation parameters s . Other model parameter is: $\beta = 0.01$. (d) is the linear-linear plot of (c), to show the peak. Note that in (c), although $\gamma = 0.25$ is smaller (than $\gamma = 0.5$), this curve moves forward relatively faster, due to the relatively larger time truncation parameter ($s = 0.1$) than the other case ($s = 0.01$).

kinetics is similar to that described by the classical, 2nd-order ADE (Fig. 8a). Note that in the numerical examples shown in Fig. 8a, both the capacity coefficient ($\beta = 0.1$) and the truncation parameter ($s = 1 \times 10^{-6}$) are relatively small. In the time tempered FADE (17),

the time drift term $\partial C/\partial t$ dominates, especially for a small capacity coefficient and truncation parameter. That is why the simulated reaction rate with different γ can be similar at the short-time region (since the impact of γ on particle waiting time has not significantly affected particle dynamics yet).

Fig. 8b shows that the increase of the capacity coefficient β decelerates the mass decline rate of reactant A . This is because a large β causes long waiting times, decreasing the mixing of reactants. In addition, Fig. 8c shows the influence of the truncation parameter s on the mass decline of reactant A . As s increases, the long waiting times decrease and the transition from the time tempered FADE (17) to asymptotic diffusion is faster. That is why the reaction rate for a large truncation parameter is similar to the 2nd-order ADE.

3.2. The open system. For the open system with a sharp interface between reactants, the volume of the mixing zone is affected by non-Fickian transport. There are two empirical methods to approximate the interaction radius R_O . First, the formula (14) can be used. The second method is numerical, where we simulate solute particle motion first, and then use the calculated spreading of plumes to modify the mixing zone volume in (14).

Examples of the first method are shown in Fig. 9. The trailing edge of the displaced reactant, B , and the product C , is apparent. The trailing edge of reactant B causes the delay of B particles behind the mean displacement, while the invading reactant A has higher opportunities to meet and react with the delaying B particles. Therefore, the tempered sub-diffusion in the open system can enhance chemical reactions, which is opposite to that in the closed system.

The above particle schemes can be refined conveniently to describe more complex reactions. For example, we can assume that only mobile particles can react. A similar assumption was used by Sanchez-Vila *et al.* [6], who showed that the immobile particles cannot be accessed by mobile particles. The simulation result is shown in Fig. 10. When only mobile reactants can react (in other words, a smaller number of particles can react), the overall reaction rate can decrease (as shown by the peak of product C in Fig. 10a and 10b), while the peak of product snapshot moves faster downstream. In addition, the hold-up

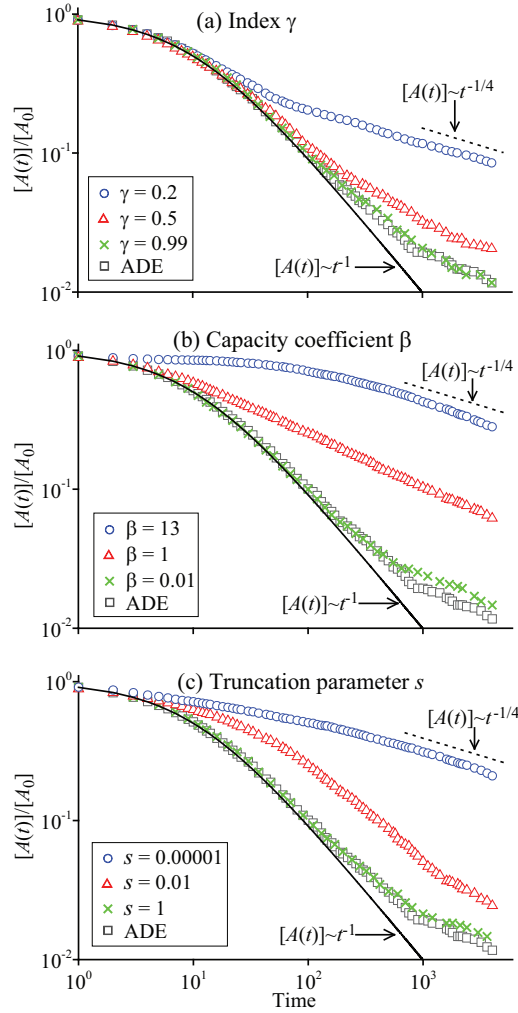


FIGURE 8. (Color online) Solutions of the bimolecular reaction, where the transport of chemicals is described by the time tempered FADE (17), for the case of well-mixed reactants. The solid line is the analytical solution by assuming a perfect mixing at all times. (a) shows the influence of scale index γ on the evolution of reactant mass decline. The other model parameters are: $\beta = 0.1$ and $s = 0.000001$. (b) shows the influence of capacity coefficient β on $[A(t)]$. The other model parameters are: $\gamma = 0.5$ and $s = 0.000001$. (c) shows the influence of truncation parameter s on $[A(t)]$. The other model parameters are: $\gamma = 0.3$ and $\beta = 2.0$. In all cases, the following parameters are used: $[A_0] = [B_0] = 0.005$, $[C_0] = 0$, $v = 0$, and $D = 0.01$.

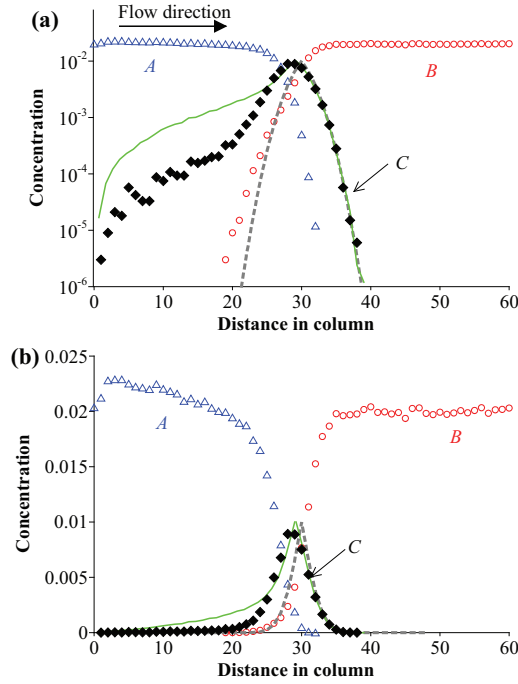


FIGURE 9. (Color online) Open system: the simulated snapshot (symbols) for A , B and C , where the diffusion is governed by the tempered time FADE (17). Model parameters are: $L = 60$, $\gamma = 0.5$, $\beta = 0.02$, $s = 0.00001$ (truncation parameter in time), $K_f = 0.5$, $v = 0.6$, $D = 0.05$, $[A_0] = [B_0] = 0.02$, $[C_0] = 0$, $T = 50$, time step $dt = 1$, and the particle number is $np = 400,000$. The dashed line denotes the analytical solution by assuming perfect mixing for the ADE model. The solid (green) line denotes the concentration of A and B in the mixing zone (without reaction). (b) is the linear-linear plot of (a).

of immobile mass near the injection point (i.e., $x = 0$) for reactant B becomes obvious, since the immobile B particles cannot move or react (Fig. 10b). Also note that, if reactions occur only between *mobile* particles, the clock time defined by the rate equation is the *mobile* time too. Therefore, the interaction radius should be increased by a factor $1/(1 + \beta)$ (which is the average time that the particle spends in motion in a unit clock/total time), although this increase is relatively small for the case shown in Fig. 10 (where $\beta = 0.1$).

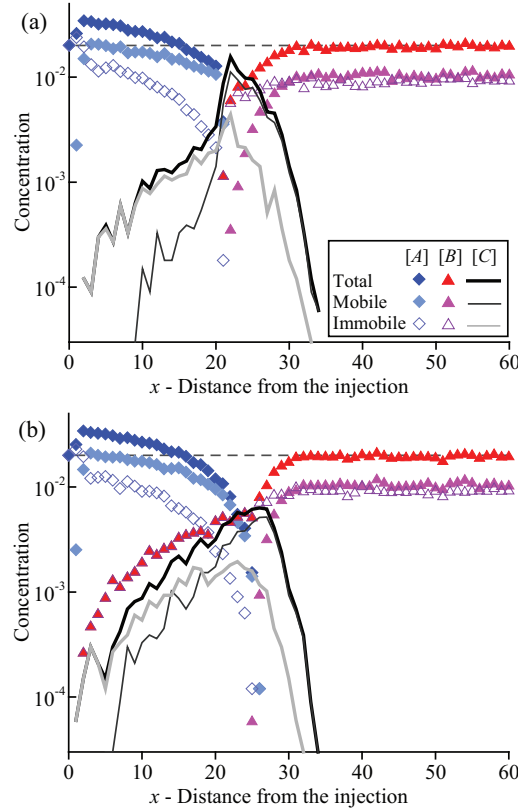


FIGURE 10. (Color online) Open system: snapshots of concentration for each chemical in each phase for the tempered time FADE controlled bimolecular reactions. In (a), particles in all phase can react; while in (b), only particles in mobile phase can react. Model parameters in both (a) and (b) are: $\gamma = 0.5$, $\beta = 0.1$, $s = 0.00001$, $v = 0.6$, $D = 0.05$, $T = 50$, $nstep=50$ (the total number of time steps), $K_f = 50$, $[A_0] = [B_0] = 0.02$, and the number of particle B is 40000. The dashed line denotes the initial concentration of reactants.

4. APPLICATIONS: LAGRANGIAN MODELING OF THE BIMOLECULAR REACTIVE TRANSPORT OBSERVED IN THE LABORATORY

We test the applicability of the above Lagrangian frameworks by simulating bimolecular reactions observed in the laboratory by different researchers. As mentioned above, the setup of laboratory experiments of bimolecular reactions typically represents open systems, where one reactant is injected into a sample column filled originally with another

reactant. In this case, the interaction radius can be a fitting parameter, or preferably, be determined using the empirical approach developed above.

The first application is shown in Fig. 11. Raje and Kapoor [5] injected 0.5 *mM* 1,2-naphthoquinone-4-sulfonic acid (NQS) solution into a 18cm-long glass column packed with uniform glass beads representing a 1-*d* porous medium. The column was originally filled with 0.5 *mM* aniline (AN) solution. The second-order, irreversible reaction between NQS and AN produces 1,2-naphthoquinone-4-aminobenzene (NQAB). The measured reaction rate constant is $K_f = 438 \text{ M}^{-1}\text{s}^{-1}$. The seepage velocity $V = 0.096 \text{ cm/s}$, the best-fit dispersion coefficient is $D = 0.03168 \text{ cm}^2/\text{s}$, and the Reynolds number $\text{Re} = 1.43$. Raje and Kapoor [5] fitted the measured breakthrough curve (BTC) for product (see symbols in Fig. 11) by assuming instantaneous and complete mixing (see the dashed line shown in Fig. 11). They found that the best-fit result overestimates the measured reaction rate, since the actual reactants are not perfectly mixed in the porous media. Here we first fit the measured BTC by assuming incomplete mixing controlled by Fickian diffusion. The best-fit BTC matches well the measured peak concentration (Fig. 11a), confirming Raje and Kapoor’s [5] conclusion that the actual mixing should be incomplete. The assumption of normal diffusion, however, underestimates the heavy early arrival (Fig. 11b). This failure motivates us to test the reaction with the tempered super-diffusion developed in this study. The best-fit parameters are: the scale index $\alpha = 1.92$, the truncation parameter $\lambda = 1 \times 10^{-5} \text{ m}^{-1}$, and the particle number $N_A^0 = 12,000$. The best-fit index α is close to 2, which we believe to be reasonable. A smaller α represents a stronger heterogeneity of the media. Here the porous medium is made of regular glass beads (with the same radius 1.5 mm), and therefore the “heterogeneity” should not be as strong as in natural media. The other parameters in (15), including K_f , $[A_0]$, L , D , and Re , are measured in the laboratory. Results show that the Lagrangian solver for reactive, tempered super-diffusive transport captures efficiently the early time tail of the BTC for product (Fig. 11).

Fig. 12 shows the second application, using the measurements by Gramling *et al.* [4]. A sodium EDTA solution (with concentration 0.02

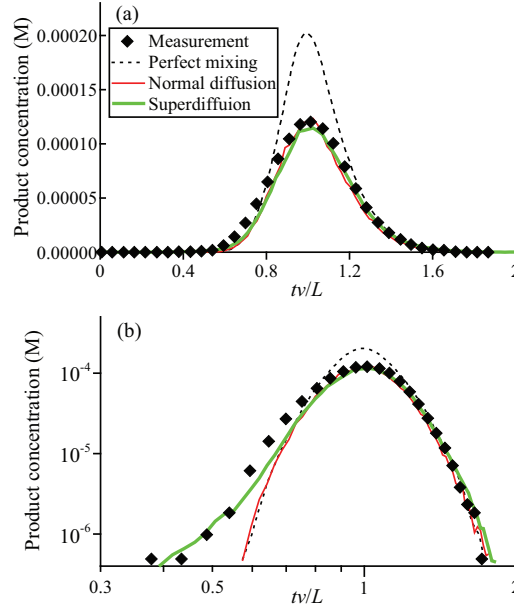


FIGURE 11. (Color online) Application Case 1: the measured product concentration (symbols) from Raje and Kapoor [5] versus the model simulated concentrations (lines). (b) is the log-log plot of (a). The dashed line is the best-fit result assuming instantaneous and complete (perfect) mixing between reactants A and B (see [5] for details). “Normal diffusion” denotes the best-fit result assuming Fickian diffusion [24]. “Superdiffusion” is the best-fit result using the Lagrangian scheme built in Sec. 2, where the transport of reactants is the tempered super-diffusion.

M) was displaced by a copper sulfate solute (with concentration $0.02 M$) filled in a thin chamber, producing copper EDTA (CuEDTA^{2-}) at the interface. This is a second-order, bimolecular reaction. The snapshot of CuEDTA^{2-} (shown by the red dots in Fig. 12) was observed. Similar to the first application, here we find that the assumption of complete mixing (shown by the dashed line in Fig. 12) over-predicts the actual reaction rate. The best-fit incomplete mixing controlled by Fickian diffusion matches well the peak concentration, but underestimates both the leading and trailing tails. The leading edge of product snapshot can be explained by the effect of tempered super-diffusion, while the trailing edge may be described by the tempered sub-diffusion.

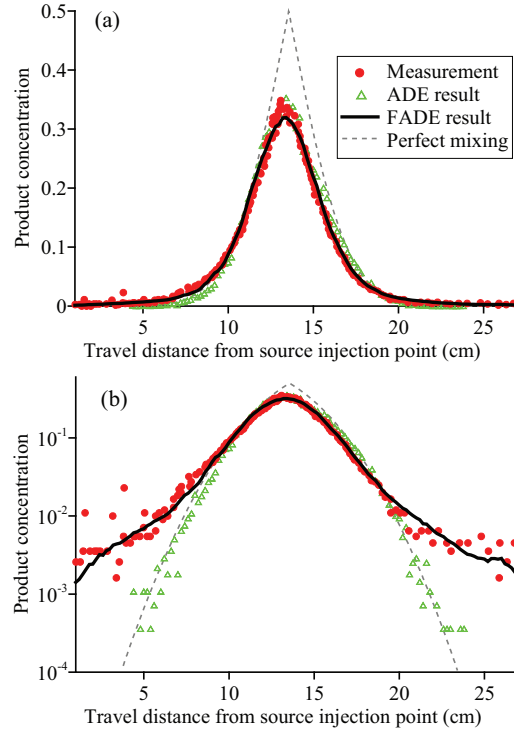


FIGURE 12. (Color online) Application Case 2: the measured product concentration (red dots) from Gramling *et al.* [4] versus the model simulated concentrations. (b) is the semi-log plot of (a), to show the tailing. The dashed line is the best-fit result assuming perfect mixing between reactants A and B . The triangles denote the best-fit result using the Lagrangian approach where the transport of reactants and product is assumed to be Fickian. The solid line denotes the best-fit result using the Lagrangian scheme built in this study, where the transport is the tempered sub/super-diffusion.

This motivates us to simulate the reaction by assuming a combination of super- and sub-diffusion, by combining the tempered super-diffusion (see Step 2 in Subsec. 2.1.2) and the tempered sub-diffusion process discussed above. Note that these two processes are independent, driven by different hydraulic properties. The mixed super- and sub-diffusion is not uncommon for transport through real media [12]. The simulation result generally captures the two tails of the observed product snapshot (Fig. 12b).

The second reactive transport exhibits more anomalous behavior than the first one. It might be due to the properties of the medium. In the second laboratory experiment, the chamber is longer ($L = 30\text{ cm}$), and it was filled with sand-sized ($1.19\text{--}1.41\text{ mm}$) grains of cryolite [4]. Compared to the glass beads used in the first experiment, the cryolite sands have irregular shapes and a relatively wider size distribution, tending to form relatively immobile domains (such as stagnant regions that are separate from the main flow paths) [6] that can delay the transport and reaction of reactants. This may explain the additional trailing edge observed in the second experiment.

It is also noteworthy that the distinction between super-diffusion and sub-diffusion is necessary. As implied by the above applications and many others [12], the two anomalous diffusions can be independent and driven by different mechanisms. Such distinction can also be useful in real applications. For example, the super-diffusion model can describe direction-dependent scaling rates (along for example fractures) (Fig. 5), while the sub-diffusion can characterize different solute behavior in different phases (mobile or immobile). To our best knowledge, no other reactive-transport code or numerical methodology has the same capability as the one developed above.

5. DISCUSSION

5.1. Future extension of the Lagrangian solver. The computational method developed in this study can be extended to capture sophisticated transport affecting chemical reactions, such as the spatial variation of velocity v and dispersion coefficient D . For example, for nonreactive transport governed by the classical second-order ADE with discrete v and D , efficient Lagrangian schemes were developed by LaBolle *et al.* [15, 16]. The Lagrangian scheme developed in this study can be combined with LaBolle’s code “RWHet” [34]. One preliminary example is shown in Fig. 13, where the transport is governed by the time tempered FADE model (17) and the interaction radius is constant. Further extensions are needed to incorporate the space tempered FADE (1) with variable parameters. In addition, the above Lagrangian scheme can be extended to capture chemical heterogeneity,

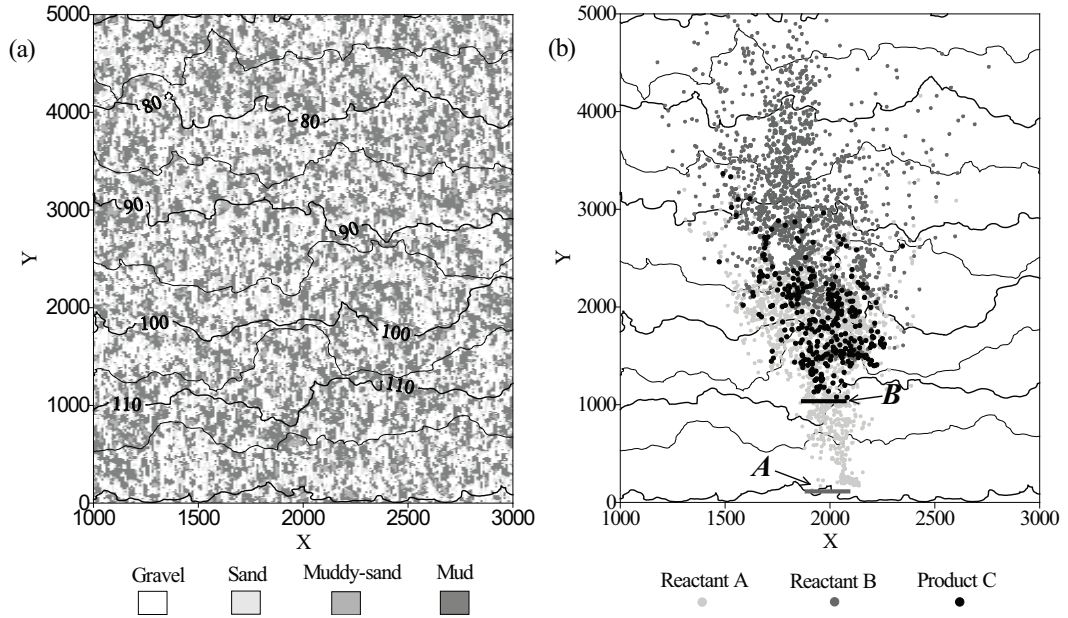


FIGURE 13. Reactive transport through a 2- d heterogeneous porous medium with space-dependent velocity and dispersion coefficient. The transport is governed by the time tempered FADE (17), while the displacement of particles crossing discrete interfaces of transport parameters is treated by the code “RWHet” [34]. (a) The hydrofacies model with 4 facies. The lines denote the simulated hydraulic head. (b) The spatial distribution of particles for bimolecular reaction $A + B \rightarrow C$. The thick, horizontal lines show the initial location of reactant A and B , respectively.

where the interaction radius can vary in space and/or time. We leave this and the above topic for a future study.

5.2. Governing equation of the dynamic process. The governing equation (1) follows the classical mass balance law [12]. Although there is no rigorous derivation of (1) for describing reactive transport combined with anomalous diffusion in porous media, similar governing equations were proposed and applied by various researchers [22, 35]. The choice of this type of model is also motivated by the work of hydrologists [36, 37, 38], who developed a similar temporally nonlocal model in the multi-rate mass transfer formulation. The same philosophy was

also applied widely by other researchers focusing on either the Brownian motion [23] or Lévy motion [13, 14] in porous media, by assuming that the stochastic process is the combination of random displacement (whose scaling limit is well known) and linear reactions. However, it is noteworthy that other forms of fractional diffusion-reaction models are also possible. For example, Henry and his colleagues [39, 40] derived rigorously the fractional reaction-diffusion equations by leading the reactive component (i.e., walkers) into the master equation, where the resultant reaction term can have a memory effect in time (i.e., loading history). The similar time-nonlocal expression for reaction was also used by Sokolov *et al.* [41] and Harman *et al.* [42] to account for the source/sink term in a time-fractional derivative model. Extensions of the above Lagrangian approach may solve the reaction-subdiffusion model with different coupling behavior, as discussed in Appendix D. In addition, the scaling limit for mixing-limited reactions may be different from that for thermodynamic rate-limited reactions [3], where the former may be developed by the technique of subordination (personnel communication, Mark M. Meerschaert, 2011). Therefore, more practical applications are needed to check the feasibility of the Lagrangian solver developed by this study. In particular, rigorous derivation of the governing equation of the scaling limit of the continuous time random walk process with well-mixed or mixing-limited reactions is still needed. We leave this open question for a future study.

6. CONCLUSIONS

This study develops computational methods to simulate the 2nd-order, bimolecular chemical reactions controlled by anomalous diffusion in heterogeneous media. The Lagrangian approach is used, where the downscaling of the transport process makes it possible to characterize both reactions and transport at the same scale. The particle-based Lagrangian approach can also efficiently simulate the incomplete mixing of reactants, which is superior to the standard Eulerian solvers that have to assume complete mixing.

A four-step Lagrangian scheme is proposed to simulate the bimolecular reaction combined with the tempered super-diffusion. In particular,

the forward reaction is controlled by the interaction radius between reactants, and the concurrent tempered super-diffusion is modeled by the Langevin equation approach. The interaction radius R can be derived for the closed system with well-mixed reactants initially, while empirical formula or fitting value for R must be used for the open system with sharp contact between reactants. This Lagrangian scheme can be extended to multi-scaling super-diffusive transport in multi-dimensional media, providing the only viable solution method for the reactive, vector fractional diffusion equation.

A time-subordination based Lagrangian scheme is then developed to simulate the bimolecular reaction combined with the tempered sub-diffusion. Chemical particles can stay in mobile or immobile phases, where the chemical reaction can occur for all particles, or for mobile particles only. In addition, chemical particles can be mobile all the time, representing the process of the standard time fractional diffusion model. The Lagrangian scheme can be applied for all cases.

Numerical results are compared to specific Eulerian solutions if available, or the known kinetics of chemical reactions. Numerical tests also show that the tempered super-diffusion enhances reaction rate by improving the mixing of reactants. The tempered sub-diffusion also helps chemical reactions by increasing the collision opportunity for reactant particles in the open system, due to the trapping of reactant particles in the immobile phase. However, in the closed system, the tempered sub-diffusion can decelerate apparently the actual reaction rate, since the actual diffusion of particles is decreased.

Applications show that the Lagrangian solver can capture efficiently the observed bimolecular reactions in sand columns. The observed breakthrough curve or snapshot for the product exhibits heavy leading or trailing tails, a typical behavior of anomalous transport that cannot be captured efficiently by normal-diffusion based models. These applications reveal the importance of considering the anomalous diffusion for reactive transport in heterogeneous systems.

Finally, it is noteworthy that this study uses a simple form of the forward reaction probability that decreases linearly with the increase of the distance between a pair of reactants. This linear reaction probability can generate the correct reaction rate, where the corresponding

interaction radius has a physical meaning [3, 28]. It is applicable to reactive transport processes observed in saturated soils. Nonlinear forms of the forward reaction probability should certainly be tested and applied, as discussed in Appendix C. In some cases, a nonlinear reaction probability may be more realistic than its linear simplification, for example, because of the influence of temperature, pressure and/or salinity on the local variation of reactions. The Lagrangian scheme developed in this study allows the forward reaction probability to be an input parameter, where the corresponding interaction radius can be fitted or even predicted.

APPENDIX A. COMPUTER GENERATION OF THE TEMPERED STABLE RANDOM VARIABLES

The numerical generation of tempered stable random variables significantly affects the computational efficiency of the Lagrangian solver developed in this study. Here we first select the modified CMS [43] method (see also [44], pages 49 ~ 50) to generate the independent stable random variables with the scale index α in $(0, 1)$ and $(1, 2)$:

$$(22) \quad Y = A \frac{\sin[\alpha(U + B)]}{[\cos(U)]^{1/\alpha}} \left| \frac{\cos[U - \alpha(U + B)]}{E} \right|^{(1-\alpha)/\alpha},$$

where U is a random variable distributed uniformly on $(-\pi/2, \pi/2)$, E is an exponential random variable with mean 1, $A = (\cos(\arctan(\beta^* \tan(\pi\alpha/2))))^{-1/\alpha}$, $B = \arctan(\beta^* \tan(\pi\alpha/2))/(1 - |1 - \alpha|)$, and β^* is the skewness ($-1 \leq \beta^* \leq 1$). We comment here that 1) the absolute value of the last term on the right-hand side of (22) must be taken; and 2) the parameter A can be ignored since the final stable random variable is $Y \times (\cos(\arctan(\beta^* \tan(\pi\alpha/2))))^{1/\alpha} = Y/A$.

The stable random variables with the maximally positive skewness were generated for the wide range of index α (Fig. 14). We found the general match to true densities. We also checked the modified CMS results against Nolan's program STABLE [45], which uses the corrected CMS approach. The convergence rate and the CPU time are almost identical (Fig. 15a,b).

We then compare the CMS method to the Pareto approach proposed by Zhang *et al.* [31]:

$$(23) \quad r = \begin{cases} U^* \phi^{1+\alpha} + \phi - \phi^{1+\alpha} + \phi/\alpha & , \quad \text{if } U^* < 1 - \phi^{-\alpha}/\alpha \\ ((1 - U^*)\alpha)^{-1/\alpha} & , \quad \text{if } U^* \geq 1 - \phi^{-\alpha}/\alpha \end{cases}$$

where U is a uniform $(0, 1)$ random number, and the parameter ϕ (with an empirical value 2.0) is the cutoff of the Pareto densities and it affects significantly the rate of convergence to the true α -stable. The α -stable random variable Y then can be obtained by shifting and re-scaling r :

$$(24) \quad Y = [r - \phi^{-1-\alpha}(\phi^2 - q^2)/2 - \phi^{-\alpha+1}/(\alpha - 1)] / [\Gamma(1 - \alpha)\cos(\pi\alpha/2)/\alpha]^{1/\alpha}.$$

The Pareto approach requires the generation of one uniform random variable at each step, while the other approaches discussed in this

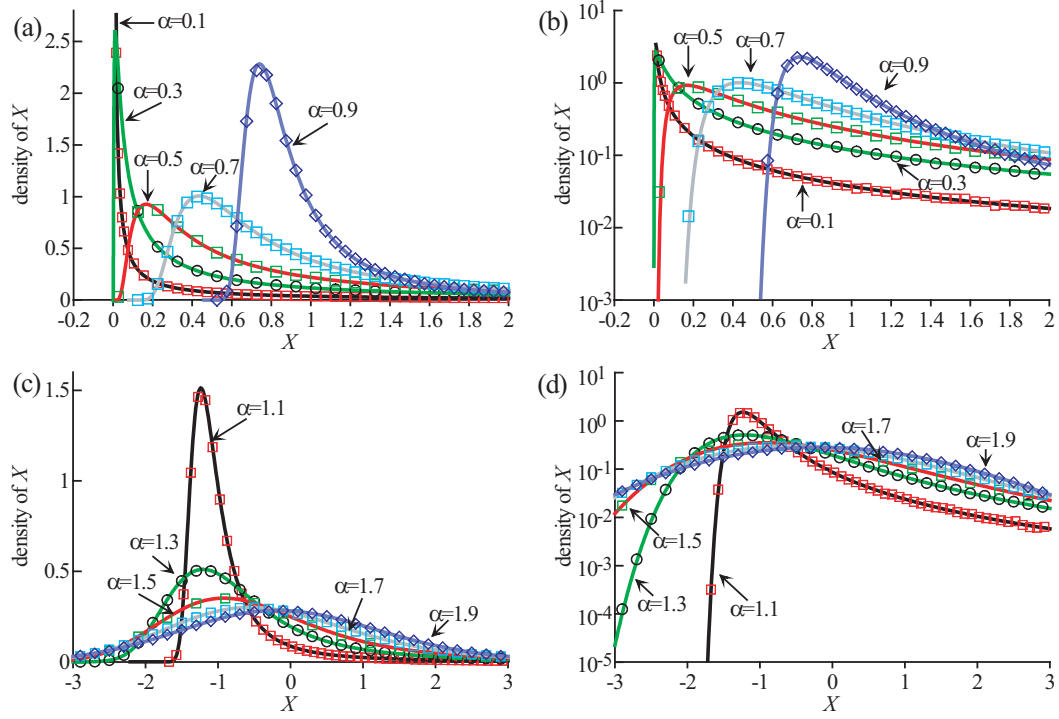


FIGURE 14. (Color online) The simulated stable density with the maximally positive skewness ($\beta = +1$) and varying index α by using the CMS method (symbols) versus the true densities (lines). 10^6 Lévy stable random variables are generated for each α . (a) $\alpha = 0.1 \sim 0.9$; (b) the semi-log plot of (a); (c) $\alpha = 1.1 \sim 1.9$; (d) the semi-log plot of (c).

appendix need to generate two independent uniform or exponential random variables (experiments show that the Pareto approach takes $\sim 50\%$ less CPU time than the other approaches). The Pareto approach can also be extended easily to generate dependent α -stable random variables, as demonstrated by Zhang *et al.* [31]. However, the random number r generated by (23) actually distributes as a Pareto with density

$$f(r) = \begin{cases} \phi^{-1-\alpha} & , \quad \text{if } \phi - \phi^{1+\alpha} + \phi/\alpha \leq r \leq \phi \\ r^{-1-\alpha} & , \quad \text{if } \phi \leq r < +\infty \end{cases}$$

which has the similar shape as the simulated density with “ $nt = 1$ ” in Fig. 15c. Only the sums of Y will be in the domain of attraction

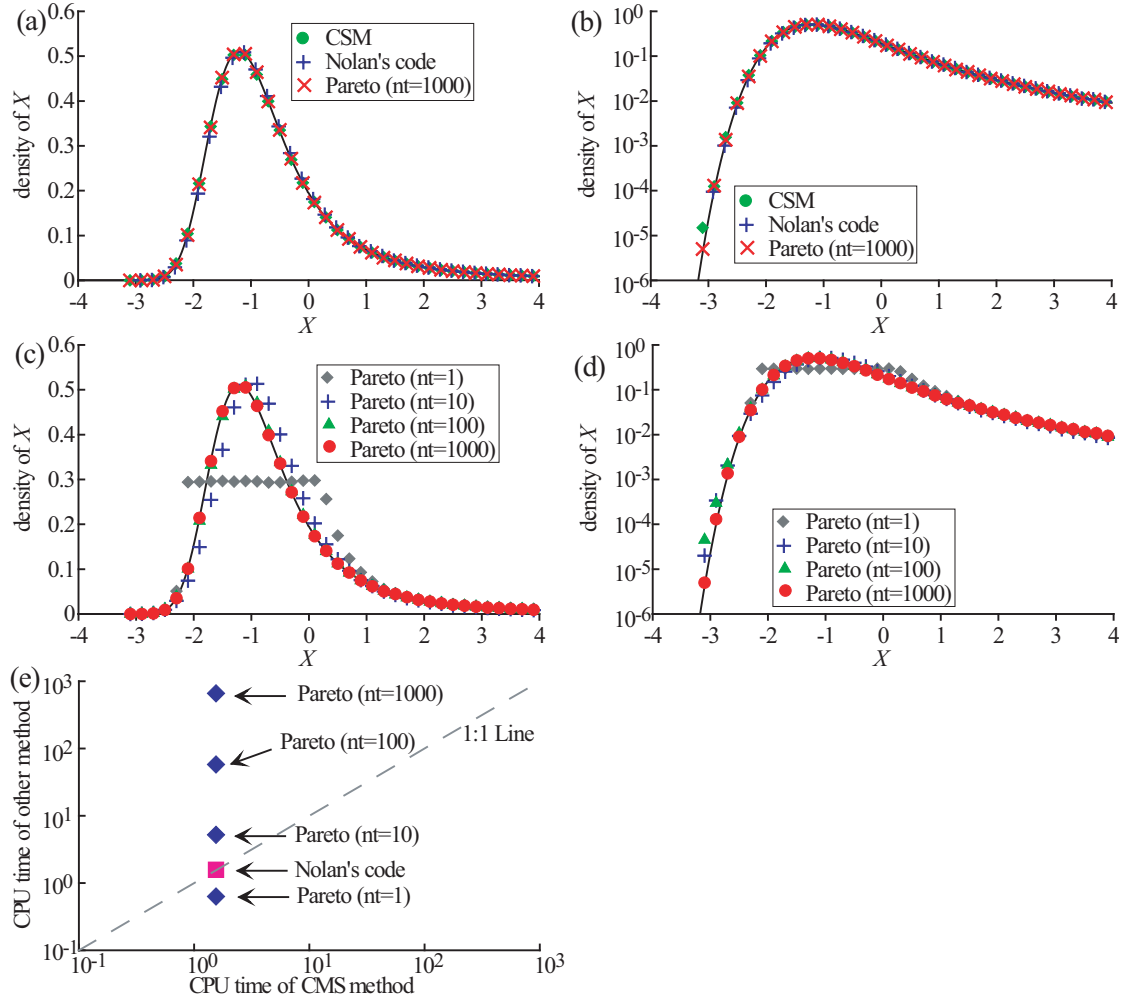


FIGURE 15. (Color online) (a) Convergence of the numerical density (symbols) generated by the modified CMS approach (22), Nolan's [45] STABLE program, and the Pareto approach (23) to the true density (line). $\alpha = 1.3$. (b) is the semi-log version of (a). (c) shows the simulated density using the Pareto approach with 4 different number of sums (indicated by the legend "nt"). (d) is the semi-log version of (c). (e) shows the CPU time (with a unit second) used by different approaches.

of an α -stable random variable $S_\alpha(1, +1, 0)$. Fig. 15(c) and (d) show that only the sums of Pareto random variables can converge to the true α -stable. Therefore, to get the same quality of convergence, the Pareto

approach (requiring the sums of multiple random variables) actually takes much more CPU time than the CMS approach (see Fig. 15(e)).

In addition, Fulger *et al.* ([46], Eq. (20)) also used the one-parameter Mittag-Leffler function to produce α -stable random variables:

$$(25) \quad Y = -\gamma_t \ln(U_1) \left[\frac{\sin(\alpha\pi)}{\tan(\alpha\pi U_2)} - \cos(\alpha\pi) \right]^{1/\alpha},$$

where U_1 and U_2 are independent uniform $(0, 1)$ random numbers, and γ_t is the scale parameter. This scheme is faster than the modified CMS method since the formula (25) takes less computation than (22) (it takes $\sim 15\%$ less CPU time in our experiments). Both Fulger *et al.*'s [46] examples and our tests (not shown here) revealed that (25) works well for $0 < \alpha < 1$. However, whether (25) works for $1 < \alpha < 2$ remains to be shown. Additionally, as pointed out by Fulger *et al.* [46], a Mittag-Leffler random variable (Y in (25)) is not stable, but a geometric stable, which needs to be re-scaled and shifted.

Numerical experiments and comparisons conducted above help us to choose the modified CMS method (22) in this study.

The next step is to generate the tempered stable random variable using the exponential rejection method of Baeumer and Meerschaert [47]. For example, to generate the α -order tempered stable random variable $d\xi_i$ in (5), we first draw a random variable $Z = D^{1/\alpha} Y$, and an exponentially distributed random variable W with mean λ^{-1} . If $W < Z$, reject and draw again; otherwise set $d\xi_i = Z + D \Delta t \alpha \lambda^{\alpha-1}$ (where Δt is the time step used in the Lagrangian solver).

To generate the γ -order tempered stable random variable $d\zeta_j$ in (20), we draw and compare $S = \beta^{1/\gamma} Y$ and W^* , where W^* is an exponentially distributed random variable with mean s^{-1} . If $W^* < S$, reject and draw S and W^* again; otherwise set $d\zeta_j = S + \beta d\tau_j \gamma s^{\gamma-1}$ (where $d\tau_j$ is the operational time used in (20)).

The simulated tempered stable densities are compared with the true densities. One example for $\alpha = 1.1$ with various truncation parameters is shown in Fig. 16.

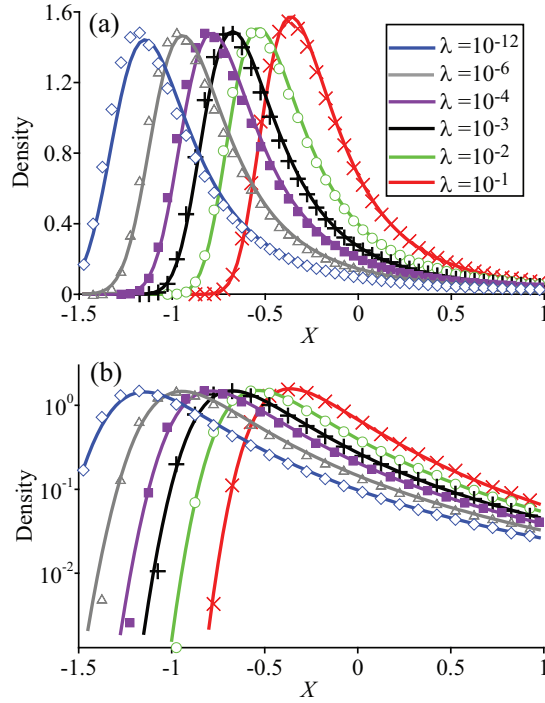


FIGURE 16. (Color online) The simulated tempered stable densities with variable truncation parameter (symbols) versus the true densities (lines). $\alpha = 1.1$. (b) is the semi-log plot of (a), to show the tailing.

APPENDIX B. IMPLICIT EULERIAN FINITE-DIFFERENCE SOLUTION OF THE SPATIOTEMPORAL TEMPERED STABLE MODEL

To cross-verify the Lagrangian description of particle motions, we develop the implicit Eulerian method to approximate the tempered stable model. Note, however, the chemical reaction term cannot be compared directly between Eulerian and Lagrangian methods, since they need not describe the same process. It is well known that if the microscopic-scale chemical reaction term is added directly into the macroscopic-scale transport model, the resultant continuum model solved by Eulerian methods overestimates significantly the reaction rate observed in the laboratory [4, 5] or approximated by Lagrangian methods [3]. Chemical reactions must be upscaled before added into the continuum model, as demonstrated recently by Sánchez-Vila *et al.* [6]. How to upscale

chemical reactions controlled by non-Fickian transport is beyond the scope of this study, and it remains an open question.

The continuum model studied here is for the conservative tracer $[A(x, t)] - [B(x, t)]$ (see Subsec. 2.2). This study considers the truncation of α -stable density in either space or time. Hence this appendix solves the following spatiotemporal tempered stable model

$$\begin{aligned}
 (26) \quad & \frac{\partial C(x, t)}{\partial t} + \beta e^{-st} \frac{\partial^\gamma}{\partial t^\gamma} [e^{st} C(x, t)] - \beta s^\gamma C(x, t) \\
 & = -V \frac{\partial C(x, t)}{\partial x} + D \left\{ e^{-\lambda x} \frac{\partial^\alpha}{\partial x^\alpha} [e^{\lambda x} C(x, t)] \right. \\
 & \quad \left. - \lambda^\alpha C(x, t) - \alpha \lambda^{\alpha-1} \frac{\partial C(x, t)}{\partial x} \right\} + m_0 \beta \frac{e^{-st} t^{-\gamma}}{\Gamma(1-\gamma)} \delta(x).
 \end{aligned}$$

Here C denotes the concentration for conservative tracers at the total (mobile + immobile) phase, and the space and time fractional derivatives are the Riemann-Liouville type. The Riemann-Liouville fractional derivative is used here, so that the shifted Grünwald approximation can be applied [47].

The model (26) can be discretized using an implicit finite difference scheme

$$\begin{aligned}
 (27) \quad & \frac{C_i^{n+1} - C_i^n}{\Delta t} + \frac{\beta e^{-st_{n+1}}}{(\Delta t)^\gamma} \sum_{k=0}^{n+1} \left[g_k e^{-st_{n-(k-1)}} C_i^{n-(k-1)} \right] + \beta s^\gamma C_i^{n+1} \\
 & = -V \frac{C_i^{n+1} - C_{i-1}^{n+1}}{h} + D \left\{ e^{-\lambda x_i} \frac{1}{h^\alpha} \sum_{j=0}^{i+1} \left[f_j e^{\lambda x_{i-(j-1)}} C_{i-(j-1)}^{n+1} \right] \right. \\
 & \quad \left. - \lambda^\alpha C_i^{n+1} - \alpha \lambda^{\alpha-1} \frac{C_i^{n+1} - C_{i-1}^{n+1}}{h} \right\} + m_0 \beta \frac{e^{-st_{n+1}} t_{n+1}^{-\gamma}}{\Gamma(1-\gamma)} \delta(x),
 \end{aligned}$$

where g_k and f_j are Grünwald weights, and Δt and h denote time and space discretization sizes, respectively. Here the one-shift Grünwald approximation [47] is used to approximate both the time (γ -order and $0 < \gamma < 1$) and space (α -order and $1 < \alpha < 2$) fractional derivatives.

By discretizing model (26) for each node (i in (27) increases from 1 to K), we obtain a linear system of equations $\mathbf{F} \mathbf{C}^{n+1} = \mathbf{C}^n + \Delta t \mathbf{S}^{n+1}$, where $\mathbf{C}^n = [C_0^n, C_1^n, C_2^n, \dots, C_K^n]^T$ and $\mathbf{C}^{n+1} =$

$[C_0^{n+1}, C_1^{n+1}, C_2^{n+1}, \dots, C_K^{n+1}]^T$. $\mathbf{F} = [F_{i,j}]$ ($i, j = 1, \dots, K-1$) is the matrix of coefficients. These coefficients are defined by:

$$F_{i,j} = \begin{cases} 0, & \text{when } j \geq i+2 \\ -\frac{\Delta t}{h^\alpha} D f_0 e^{\lambda h}, & \text{when } j = i+1 \\ 1 + \frac{\beta g_0}{(\Delta t)^{\gamma-1}} - \Delta t \beta s^\gamma + V \frac{\Delta t}{h} - \Delta t D \left[\frac{f_1}{h^\alpha} - \lambda^\alpha - \alpha \lambda^{\alpha-1} \frac{1}{h} \right], & \text{when } j = i \\ -V \frac{\Delta t}{h} - \Delta t D \left[\frac{1}{h^\alpha} f_2 e^{-\lambda h} + \alpha \lambda^{\alpha-1} \frac{1}{h} \right], & \text{when } j = i-1 \\ -\Delta t D \frac{1}{h^\alpha} f_{i-(j-1)} e^{-\lambda(i-j)h}, & \text{when } j \leq i-2 \end{cases}$$

while $F_{0,0} = 1$, $F_{0,j} = 0$ for $j = 1, \dots, K$, $F_{K,K} = 1$, $F_{K,K-1} = -1$, and $F_{K,j} = 0$ for $j = 0, \dots, K-2$.

The stable criterion of the above finite-difference numerical scheme is analyzed using the Greschgorin theorem [48]. The eigenvalues of the matrix \mathbf{F} are in the disks centered at $F_{i,i}$ with radius $r_i = \sum_{k=0, k \neq i}^K F_{i,k}$. Firstly, we have

(28)

$$F_{i,i} - r_i = 1 + \frac{\beta g_0}{(\Delta t)^{\gamma-1}} - \Delta t \beta s^\gamma + \Delta t D \lambda^\alpha - \frac{\Delta t D}{h^\alpha} \sum_{j=0}^{i+1} [f_{i-j+1} e^{-\lambda(i-j)h}].$$

To meet the criterion of $A_{i,i} - r_i > 1$, the following formula must be satisfied:

$$(29) \quad \frac{\beta g_0}{(\Delta t)^{\gamma-1}} - \Delta t \beta s^\gamma + \Delta t D \lambda^\alpha - \frac{\Delta t D}{h^\alpha} \sum_{j=0}^{i+1} [f_{i-j+1} e^{-\lambda(i-j)h}] > 0.$$

which requires

$$(30) \quad \Delta t < \beta^{1/\gamma} \left[\frac{1}{h^\alpha} D e^{\lambda h} - D \lambda^\alpha + \beta s^\gamma \right]^{-1/\gamma}.$$

Here the Grünwald weights $g_0 = 1$, $f_0 = 1$, $f_1 = -\alpha$ (so $-2 < f_1 < -1$), $f_2 = \alpha(\alpha-1)/2 > 0$, and $f_i > 0$ for $i > 2$.

Secondly, we have

(31)

$$\begin{aligned} F_{i,i} + r_i = & 1 + \frac{\beta g_0}{(\Delta t)^{\gamma-1}} - \Delta t \beta s^\gamma + \Delta t D \lambda^\alpha + 2V \frac{\Delta t}{h} + 2\Delta t D \alpha \lambda^{\alpha-1} \frac{1}{h} \\ & - \Delta t D \frac{f_1}{h^\alpha} + \frac{\Delta t}{h^\alpha} D f_0 e^{\lambda h} + \frac{\Delta t}{h^\alpha} D f_2 e^{-\lambda h} + \Delta t D \frac{1}{h^\alpha} \sum_{j=0}^{i-2} [f_{i-j+1} e^{-\lambda(i-j)h}]. \end{aligned}$$

The formula (30) shows that

$$(32) \quad \frac{\beta}{(\Delta t)^{\gamma-1}} - \Delta t \beta s^\gamma + \Delta t D \lambda^\alpha > 0 ,$$

implying that the summation of the 2nd, 3rd, and 4th terms on the right hand side of (31) is larger than zero. In addition, given the properties of the Grünwald weights f_i , we find that all the remaining terms on the right hand side of (31) are larger than zero. Therefore,

$$(33) \quad F_{i,i} + r_i > 1 .$$

Hence the magnitude of eigenvalues of \mathbf{F} are no less than 1 if the time step Δt is small enough to meet the criterion of (30). The spectral radius of the inverse matrix \mathbf{F}^{-1} is no larger than 1 and any error in \mathbf{C}^{n+1} is not magnified. Hence the above Eulerian numerical scheme is conditionally stable.

The above Eulerian scheme has been used to cross verify the Lagrangian solutions developed in Sec. 2 and Sec. 3. A general match for solutions can be found for the two different numerical solvers (see Fig. 1, Fig. 7, and the corresponding explanation in the text).

APPENDIX C. THE NONLINEAR FUNCTIONAL FORM FOR THE FORWARD REACTION PROBABILITY

The forward reaction probability P_f^* defined by (7) decreases linearly with the increase of distance between each pair of reactants. Can this simple linear probability generate an appropriate reaction rate? Is it possible to replace (7) by nonlinear reaction probabilities so that P_f^* looks more realistic? This appendix focuses on these questions.

For illustration purposes, we consider the power-law form for P_f^* by generalizing (7):

$$(34) \quad P_f^*(t) = 1 - \frac{|y_{A,i}(t) - y_{B,j}(t)|^a}{(R^*)^a} ,$$

where $a > 0$. This appendix uses R^* to denote the interaction radius, to distinguish it from the other interaction radius used in the main text. Other nonlinear P_f^* , such as the exponential or logarithmic function, can also be used by following the argument below.

As explained in Subsec. 2.1.3, there are two sub-steps before a reaction can occur. First, the pair of reactants should be closer than

the interaction radius R^* , a “standard” criterion used by different researchers [3, 28]. The probability of this sub-step (denoted as $P_1(t)$), which characterizes the number of reactant pairs in R^* , can be approximated by [24]

$$(35) \quad P_1(t) \approx \frac{2R^*}{L/N_A(t)},$$

where we assume uniform initial concentrations for reactants. Here the term $R^*/[L/N_A(t)]$ in (35) approximates the proportion of reactant A within R^* , and the factor “2” in (35) accounts for the fact that the reactant B can be located on both sides of a A particle (hence doubling the reaction probability).

During the 2nd sub-step (see Subsec. 2.1.3), a uniform $[0, 1]$ random number is compared to (34), to determine whether the reaction can occur. The corresponding average probability is

$$(36) \quad P_2(t) \approx \frac{1}{R^*} \int_0^{R^*} \left[1 - \left(\frac{x}{R^*} \right)^a \right] dx.$$

The product of the two sub-probabilities defined by (35) and (36) (which are independent) leads to the average forward reaction probability

$$(37) \quad \bar{P}_f(t) \approx \frac{2a}{1+a} \frac{R^*}{L/N_A(t)}.$$

To generate the correct reaction rate (or rate equation), the radius R^* should be defined properly.

For the case with equal initial concentrations $[A_0] = [B_0]$, the rate equation reads and approximates

$$(38) \quad \frac{\partial[A(t)]}{\partial t} = -K_f [A(t)]^2 \approx \frac{\Delta[A(t)]}{\Delta t},$$

with a small time step Δt . On the other hand, the probability $\bar{P}_f(t)$ (37) can also be regarded as the proportion of reacted particles at time t :

$$(39) \quad \bar{P}_f(t) = \frac{|\Delta[A(t)]|}{[A(t)]}.$$

Combining (37), (38) and (39), we find that when the radius R^* takes the form

$$(40) \quad R^* = \frac{1+a}{2a} \frac{K_f [A(t)] L \Delta t}{N_A(t)},$$

the power-law function (34) generates the correct reaction rate.

We test systematically the applicability of the power-law function (34) coupled with the interaction radius R^* (40). Several examples are shown in Fig. 17. For comparison purposes, we first use the original interaction radius R_C defined by (9), followed by R^* defined by (40). When R_C is used, the case of $a = 1$ (Fig. 17a) successfully estimates the analytical evolution of reactant and product concentrations, verifying the applicability of the linear reaction probability used in the main text. The other two cases either underestimate the reaction rate ($a = 0.5$, Fig. 17b) or overestimate it ($a = 2.0$, Fig. 17c), due to either the decreased chance for reaction (when $a < 1$) or the enhanced probability for reaction (when $a > 1$) within the range of R_C . Only when the interaction radius is scaled properly, as expressed by (40), will the simulated reaction rate be correct (Fig. 17d,e).

Based on (13), we can link the interaction radius R^* (for the power-law function (34)) and the interaction radius R_C (for the linear function (7)):

$$(41) \quad R^* = \frac{1+a}{2a} R_C.$$

Eq. (41) (depicted in Fig. 18a) also implies an efficient way to define the interaction radius for an arbitrary form of reaction probability. The cumulative reaction probability, which is equal to the area underlying the reaction probability curve shown in Fig. 18b, should remain constant. Such area is known as $R_C/2$ for the case of $a = 1$. This leads to the conversion between R_C and the new interaction radius R^* for an arbitrary (i.e., logarithmic or exponential) reaction probability.

When $a = 1$, $R^* = R_C$, and the nonlinear reaction probability (34) reduces to the linear one (7). Hence the linear reaction probability (7) coupled with the interaction radius R_C (9) does generate the correct reaction rate. Most importantly, the predictable interaction radius R_C has a clear physical meaning, as shown by Pogson *et al.* [28] and Benson and Meerschaert [3].

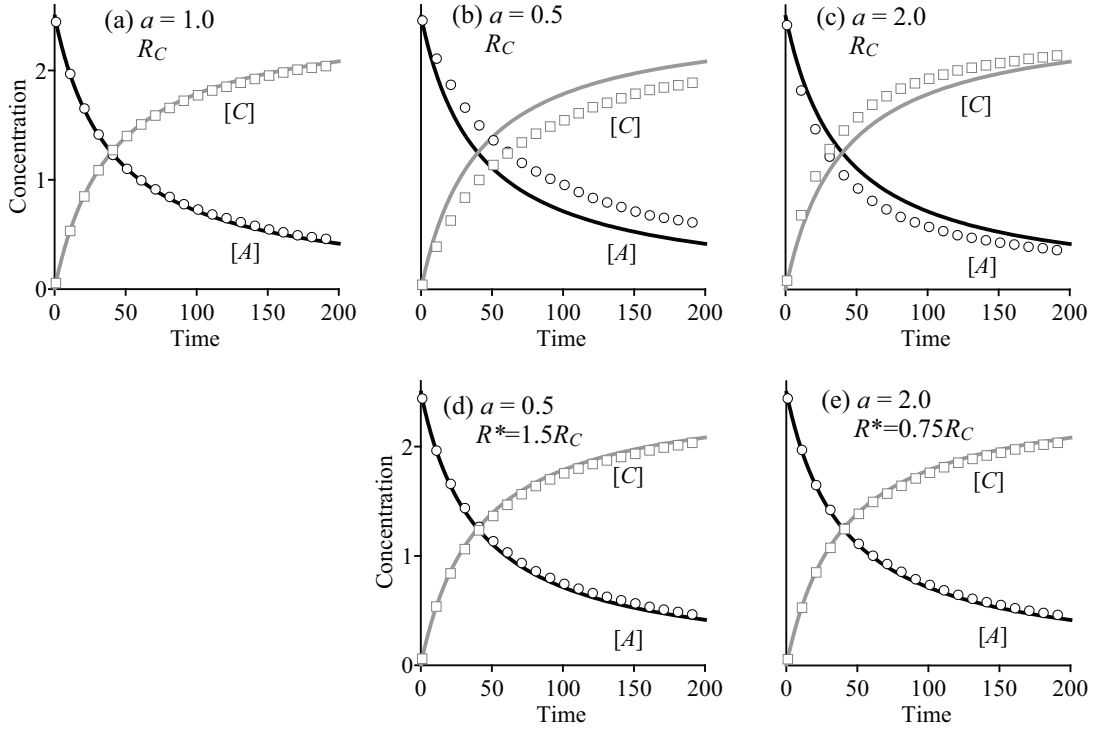


FIGURE 17. Numerical verification - evolution of reactant A and product C : analytical solutions (lines) versus the Lagrangian solutions (symbols). The interaction radius used in (a), (b) and (c) is R_C defined by (9), while the updated interaction radius R^* defined by (40) is used in (d) and (e). Note that (a), (d) and (e) are almost identical. The legend “ a ” denotes the exponent “ a ” in the power-law form of reaction probability (34).

To draw a conclusion, this appendix shows that the simple linear reaction probability (7) is applicable. The more realistic, nonlinear reaction probability can also be used in our Lagrangian solver.

APPENDIX D. LAGRANGIAN SIMULATION OF THE FULLY COUPLED, PARTIALLY COUPLED, AND DECOUPLED REACTION AND SUBDIFFUSION

This appendix extends one of the Lagrangian algorithms developed in the main text (Subsec. 3.1) to simulate the reaction-subdiffusion with different coupling behavior. Sokolov *et al.* [41] found that, for the simple monomolecular conversion $A \rightarrow B$, the parameters of the

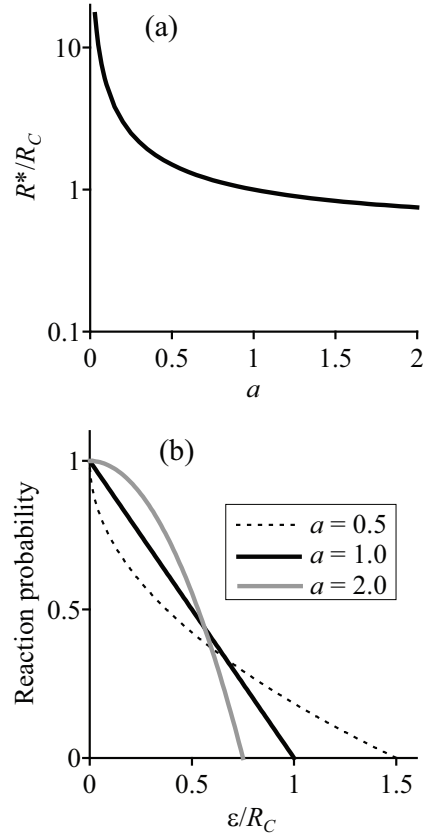


FIGURE 18. (a) Scaling of the interaction radius (R^*) for each power-law exponent a , as expressed by (41). (a) The forward reaction probability distribution expressed by $f(\varepsilon) = 1 - (\varepsilon/R_C)^a$.

reaction (i.e., the conversion rate) influence the diffusion term in the governing equation of reaction-subdiffusion. Henry *et al.* [39] derived three mesoscopic models for subdiffusion with linear reaction dynamics, including Sokolov *et al.*'s model. In the following we first introduce briefly each model, and then build and test the Lagrangian solver.

D.1. Model III - The fully coupled reaction and subdiffusion.

Model III in [39] is the same as the coupled reaction-subdiffusion model proposed by Sokolov *et al.* [41]:

$$(42) \quad \frac{\partial n}{\partial t} = D(\gamma) e^{\pm kt} \mathcal{D}^{1-\gamma} \left(e^{\mp kt} \frac{\partial^2 n}{\partial x^2} \right) \pm kn,$$

where n is the number density of random walkers, $D(\gamma)$ is the diffusivity, k is the conversion rate (either negative or positive), and the operator $\mathcal{D}^{1-\gamma}$ denotes the Riemann-Liouville fractional derivative of order $1 - \gamma$ (where $0 < \gamma < 1$).

Henry *et al.* [39] built model (42) using the Master equation approach, where available walkers are added or removed at a constant rate during the time interval between jumps. Their description of particle dynamics motivates us to revise the six-step time-subordination approach proposed in Subsec. 3.1. In *Step 1*, the time Langevin equation (20) is revised as

$$(43) \quad dT_j = d\zeta_j,$$

where the operational time is no longer part of the real time (since the jump now is instantaneous). The 1 : 1 short lines on the right half of Fig. 6 representing the operational time, therefore, become vertical lines, since they do not affect the real time t any more. The particle displacement in the operational time calculated in *Step 3* remains unchanged, with a pre-defined operational time step. In *Step 5*, we now calculate the first-order decay with the rate k . The other steps remain unchanged. Results show that the Lagrangian solution generally matches the exact solution (Fig. 19).

It is also noteworthy that both Henry *et al.* [39] and Sokolov *et al.* [41] found that the coupled reaction-subdiffusion (42) can be solved analytically. Assuming $n(x, t) = e^{kt} y(x, t)$, Henry *et al.* [39] found that model (42) converts to the following subdiffusion model

$$(44) \quad \frac{\partial y}{\partial t} = D \mathcal{D}^{1-\gamma} \frac{\partial^2 y}{\partial x^2},$$

whose analytical solution is well-known [7]. This implies that reaction and subdiffusion can be calculated independently, or in other words, the conversion actually does not affect directly the motion of each walker. After rewriting (44) as

$$\frac{\partial^\gamma y}{\partial t^\gamma} = D \frac{\partial^2 y}{\partial x^2},$$

and applying the time-Langevin analysis [32], we find that the particle diffuses in the operational time and decays in the waiting time. This conclusion supports the above extended time-subordination approach.

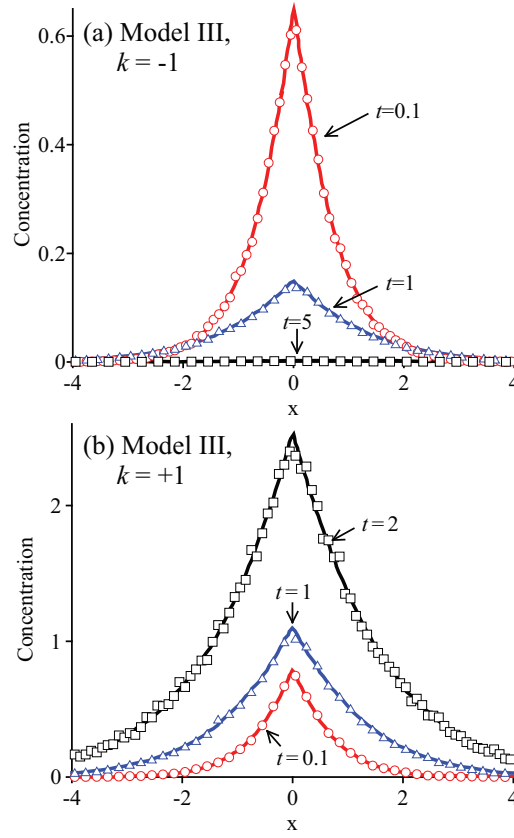


FIGURE 19. (Color online) Model III: The concentration snapshot for A particles simulated by the Lagrangian approach (symbols) versus the true solution (lines) [39], at various dimensionless times with $D = 1$, $\gamma = 0.5$, and $k = -1$ (a) and $k = +1$ (b), respectively. The instantaneous point source of reactant A is located at the origin $x = 0$.

It is also consistent with Henry *et al.*'s description of the stochastic process underlying model (42) [39].

D.2. Model II - The partially coupled reaction and subdiffusion. Model II in [39] takes the form

$$(45) \quad \frac{\partial n}{\partial t} = D(\gamma) \mathcal{D}^{1-\gamma} \left[\frac{\partial^2 n}{\partial x^2} \right] \pm \frac{k}{1 \pm k} \left(\frac{\gamma}{k \Gamma(1-\gamma) \tau_D^\gamma} \right) \mathcal{D}^{1-\gamma} n,$$

where τ_D is the characteristic mesoscopic time scale, and Γ is the gamma function. We call (45) the “partially coupled” model since the constant k is no longer located inside of the fractional derivative.

When deriving model (45), Henry *et al.* [39] added or removed a constant portion of the available walkers instantaneously at the start of each jump. Hence we calculate particle conversion in the operational time, the same time domain where particles make their movement in space. The above six-step time-subordination approach only needs to be revised slightly, where the reaction occurs in the operational time in *Step 5*. Fig. 20 shows that the Lagrangian solution generally matches the analytical solution for model (45). The particle mass described by Model II (45) declines slower to zero than that for Model III (42), simply due to the relatively short operational time compared to the waiting time defined in the time subordinated process.

D.3. Model I - The decoupled reaction and subdiffusion. Model I in [39] is called the decoupled reaction and subdiffusion model by Sokolov *et al.* [41]:

$$(46) \quad \frac{\partial n}{\partial t} = D(\gamma) \mathcal{D}^{1-\gamma} \left[\frac{\partial^2 n}{\partial x^2} \right] \pm kn,$$

where the reaction and diffusion look independent.

To derive model (46), Henry *et al.* [39] added or removed a fraction of walkers at a constant rate in time, independent of the diffusion process. We comment that Model I actually contains a time-nonlocal conversion, since the fractional integral operator can act on the reaction term in (46), similar to the memory effect of rainfall on hillslope flow proposed in [42]. To account for the memory effect, we need to add all the previous contribution of the source/sink term (at each time that is independent of particle displacement) on the current solution in the Lagrangian solver. This results in the numerical solution that generally matches the exact solution (Fig. 21a). The case for Model I considered by Sokolov *et al.* [41] (where a numerical approach was used to solve Model I (46)) is also simulated and shown in Fig. 21b. Compared to Model III expressed by (42), the decline of particle mass at the origin is relatively slow for Model I.

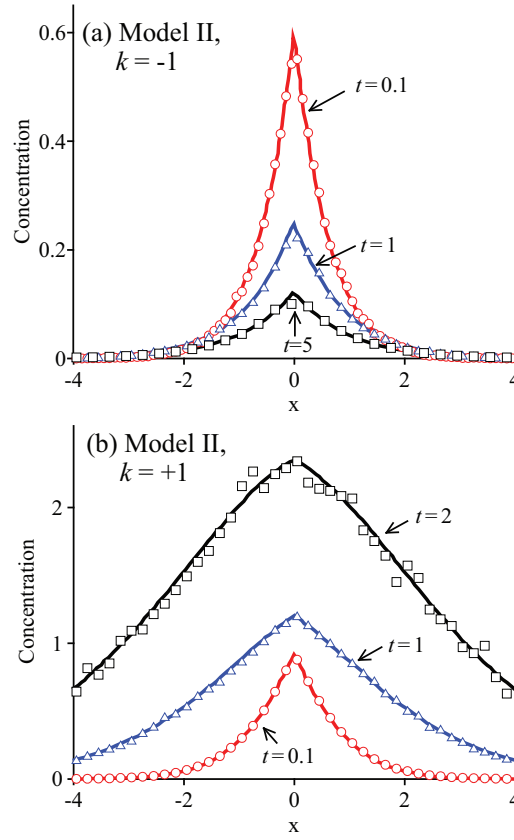


FIGURE 20. (Color online) Model II: The concentration snapshot for A particles simulated by the Lagrangian approach (symbols) versus the true solution (lines) [39], at various dimensionless times. All the model parameters are the same as those used in Figure 19. The only difference is the model itself.

D.4. The dynamically coupled reaction and subdiffusion model. In hydrological processes, the reaction and anomalous diffusion can be dynamically coupled. For example, the precipitation occurring in a porous medium can change the geometry or pore connectivity of the medium, resulting in a significant variation of flow properties. Particle transport behavior is therefore affected. Such process can be simulated by the Lagrangian algorithm developed in this study, where the dispersion component (such as the diffusivity and scale index) varies with reaction. Preliminary extensions of the Lagrangian algorithm are

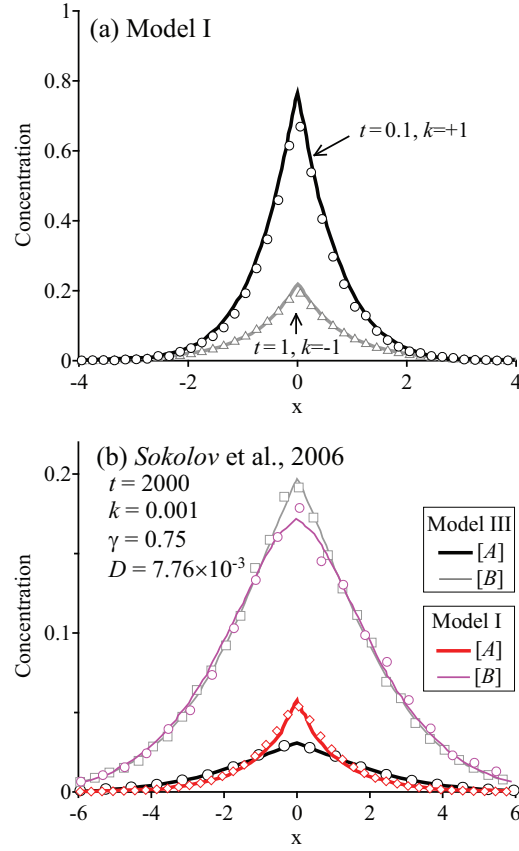


FIGURE 21. (Color online) (a) The concentration snapshot for A particles simulated by the Lagrangian approach (symbols) versus the true solution (lines) [39] at time $t = 1$ and $k = -1$, and time $t = 0.1$ and $k = +1$, respectively. The other parameters are the same as those used in Fig. 19. (b) The concentration distribution for A and B particles simulated by the Lagrangian approach (symbols) versus the analytical or numerical solutions (lines) in Sokolov *et al.* [41], for Model I and III.

conducted (not shown here), and laboratory experiments are needed to check and refine the computational method.

To draw a conclusion, the Lagrangian algorithm developed in this study can be extended to simulate the coupled reaction and subdiffusion.

REFERENCES

- [1] M. Dentz, T. Le Borgne, A. Englert, and B. Bijeljic, *J. Contam. Hydrol.* **120-21**, 1 (2011).
- [2] O. A. Cirpka, *J. Contam. Hydro.* **58**, 261 (2002).
- [3] D. A. Benson and M. M. Meerschaert, *Water Resour. Res.* **44**, W12202 (2008).
- [4] C. M. Gramling, C. F. Harvey, and L. C. Meigs, *Environ. Sci. Technol.* **36**, 2508 (2002).
- [5] D. Rajee and V. Kapoor, *Environ. Sc. Technol.* **34**, 1234 (2000).
- [6] X. Sanchez-Vila, D. Fernández-Garcia, and A. Guadagnini, *Water Resour. Res.* **46**, W12510 (2010).
- [7] R. Metzler, and J. Klafter, *Phys. Rep.* **339(1)**, 1 (2000).
- [8] J. H. Cushman, B. X. Hu, and T. R. Ginn, *J. Statis. Phys.* **75(5/6)**, 859 (1994).
- [9] J. H. Cushman, *Dynamics of Fluids in Hierarchical Porous Media* (Academic Press, San Diego, CA, 1990), p. 505.
- [10] B. Berkowitz, A. Cortis, M. Dentz, and H. Scher, *Review Geophys.* **44(2)**, RG2003 (2006).
- [11] S. P. Neuman and D. M. Tartakovsky, *Adv. Water Resour.* **32**, 670 (2009).
- [12] Y. Zhang, D. A. Benson, and D. M. Reeves, *Adv. Water Res.* **32**, 561 (2009).
- [13] Y. Edery, H. Scher, and B. Berkowitz, *Geophys. Res. Lett.* **36**, GL036381 (2009).
- [14] Y. Edery, H. Scher, and B. Berkowitz, *Water Resour. Res.* **46**, W07524 (2010).
- [15] E. M. LaBolle, G. E. Fogg, and A. F. B. Tompson, *Water Resour. Res.* **32**, 393 (1996).
- [16] E. M. LaBolle, J. Quastel, G. E. Fogg, and J. Gravner, *Water Resour. Res.* **36**, 651 (2000).
- [17] R. Metzler, E. Barkai, and J. Klafter, *Europhys. Lett.* **46(4)**, 431 (1999).
- [18] R. Metzler and J. Klafter, *J. Phys. A* **37**, R161 (2004).
- [19] A. Cartea and D. Del-Castillo-Negrete, *Phys. Rev. E* **76(4)**, 041105 (2007).
- [20] D. Del-Castillo-Negrete, *Phys. Rev. E* **79(3)**, 031120 (2009).
- [21] M. M. Meerschaert, Y. Zhang, and B. Baeumer, *Geophys. Res. Lett.* **35**, L17403 (2008).
- [22] D. Bolster, D. A. Benson, T. Le Borgne, and M. Dentz, *Phys. Rev. E* **82**, 021119 (2010).
- [23] R. Erban and S. J. Chapman, *Phys. Bio.* **6**, 046001 (2009).
- [24] Y. Zhang, Lagrangian simulation of bimolecular reactions (2011). Preprint available at <http://www.dri.edu/yong-zhang?start=3>
- [25] P. M. Oates and C. F. Harvey, *Exp. Fluids* doi:10.1007/s00348-006-0184-z (2006).
- [26] Y. Zhang, *J. Statis. Phys.* **139**, 915 (2010).
- [27] M. M. Meerschaert and H. P. Scheffler, *J. Appl. Probab.* **41(3)**, 623 (2004).

- [28] M. Pogson, R. Smallwood, E. Qvarnstrom, and M. Holcombe, *BioSystems* **85**, 37 (2006).
- [29] T. D. Scheibe, A. M. Tartakovsky, Y. Fang, and G. D. Redden, *EOS Trans. AGU* **87(52)**, B53B-0347 (2006).
- [30] Y. Zhang, B. Baeumer, and D. M. Reeves, *Geophys. Res. Lett.* **37**, L11405 (2010).
- [31] Y. Zhang, D. A. Benson, M. M. Meerschaert, E. M. LaBolle, and H.-P. Schefler, *Phys. Rev. E* **74**, 026706 (2006).
- [32] Y. Zhang, M. M. Meerschaert, and B. Baeumer, *Phys. Rev. E* **78**, 036705 (2008).
- [33] M. Magdziarz and A. Weron, *Phys. Rev. E* **75**, 016708 (2007).
- [34] E. M. LaBolle, *RWHet: Random Walk Particle Model for Simulating Transport in Heterogeneous Permeable Media* (User's Manual and Program Documentation, University of California, Davis, CA, 2006).
- [35] B. Baeumer, M. Kovács, and M. M. Meerschaert, *Comput. Math. Appl.* **55**, 2212 (2008).
- [36] M. De. Simoni, J. Carrera, X. Sánchez-Vila, and A. Guadagnini, *Water Resour. Res.* **41**, W11410 (2005).
- [37] L. D. Donado, X. Sánchez-Vila, M. Dentz, J. Carrera, and D. Bolster, *Water Resour. Res.* **45**, W11402 (2009).
- [38] M. Willmann, J. Carrera, X. Sánchez-Vila, O. Silva, and M. Dentz, *Water Resour. Res.* **46**, W07512 (2009).
- [39] B. I. Henry, T. A. M. Langlands, and S. L. Wearne, *Phys. Rev. E* **74(3)**, 031116 (2006).
- [40] T. A. M. Langlands and B. I. Henry, *Phys. Rev. E* **81(5)**, 051102 (2010).
- [41] I. M. Sokolov, M. G. W. Schmidt, and F. Sagués, *Phys. Rev. E* **73(3)**, 031102 (2006).
- [42] C. J. Harman, D. M. Reeves, B. Baeumer, and M. Sivapalan, *J Geophy. Res.* **115**, F00A08 (2010).
- [43] J. M. Chambers, C. L. Mallows, and B. W. Stuck, *J. Amer. Statist. Assoc.* **71(354)**, 340 (1976).
- [44] A. Janicki and A. Weron, *Simulation and Chaotic Behavior of α -stable Stochastic Processes* (Marcel Dekker, Inc., New York, 1994), p. 255.
- [45] J. P. Nolan, *Commun. Statist.-Stochastic Models* **13(4)**, 759 (1997). (The program STABLE is available from J. P. Nolan's website: academic2.American.edu/~jpnolan)
- [46] D. Fulger, E. Scalas, and G. Germano, *Phys. Rev. E* **77**, 021122 (2008).
- [47] B. Baeumer and M. M. Meerschaert, *J. Comput. Appl. Math.* **233**, 2438 (2010).
- [48] E. Isaacson and H. B. Keller, *Analysis of Numerical Methods* (Wiley, New York, 1966), p. 153.

YONG ZHANG, DESERT RESEARCH INSTITUTE, LAS VEGAS, NV 89119

E-mail address: Yong.Zhang@dri.edu

CHARALAMBOS PAPELIS, DEPARTMENT OF CIVIL ENGINEERING, NEW MEX-
ICO STATE UNIVERSITY, LAS CRUCES, NM 88003

E-mail address: lpapelis@nmsu.edu